Remote Sensing of Environment 301 (2024) 113920

Contents lists available at ScienceDirect

Remote Sensing of Environment

journal homepage: www.elsevier.com/locate/rse

Inter-comparison of melt pond products from optical satellite imagery

Sanggyun Lee [a,b,*], Julienne Stroeve [b,c,d], Melinda Webster [e], Niels Fuchs [f], Donald K. Perovich [g]

[a] Industrial Environment Cell, Research Institute of Industrial Science and Technology (RIST), Pohang 37673, South Korea
[b] Centre for Polar Observation and Modelling, University College London, Earth Sciences, 5 Gower Place, London WC1E 6BS, United Kingdom
[c] Centre for Earth Observation Science, University of Manitoba, Winnipeg, MT, MB R3T 2N2, Canada
[d] National Snow and Ice Data Center (NSIDC), University of Colorado, Boulder, CO 80309, USA
[e] Polar Science Center, Applied Physics Laboratory, University of Washington, Seattle, WA 98105-6698, USA
[f] Centre for Earth System Sustainability, Institute of Oceanography, Universität Hamburg, Hamburg 20146, Germany
[g] Thayer School of Engineering, Dartmouth College, Hanover, HN 03755, USA

ARTICLE INFO

Keywords:
Melt pond
Sea ice
Optical sensor
Remote sensing

ABSTRACT

Given the importance that melt ponds have on the energy balance of summer sea ice, there have been several efforts to develop pan-Arctic datasets using satellite data. Here we intercompare three melt pond data sets that rely on multi-frequency optical satellite data. Early in the melt season, the three data sets have similar spatial patterns in melt pond fraction, but this agreement weakens as the melt season progresses despite relatively high interannual correlations in pond fractions between the data products. Most of the data sets do not exhibit trends towards increased melt pond fractions from 2002 to 2011 despite overall Arctic warming and earlier melt onset. Further comparisons are made against higher resolution optical data to assess relative accuracy. These comparisons reveal the challenges in retrieving melt ponds from coarse resolution satellite data, and the need to better discriminate between leads, small open water areas and melt ponds. Finally, we assess melt pond data sets as a function of ice type and how well they correlate with surface albedo. As expected, melt pond fractions are negatively correlated with surface albedo, though the strength of the correlation varies across products and regions. Overall, first-year ice has larger melt pond fractions than multi-year ice.

1. Introduction

Melt ponds are a dominant feature of Arctic sea ice in summer. During advanced melt they can occupy up to 50 to 60% of the sea ice area (Fetterer and Untersteiner, 1998; Eicken et al., 2004). Since the presence of melt ponds greatly reduces the summer sea ice albedo, they play a significant role in controlling the sea ice energy balance (Perovich et al., 2007; Nicolaus et al., 2010). Melt ponds also allow more light to enter the upper ocean than bare or snow-covered sea ice, enhancing under-ice algae blooms (e.g. Horvat et al., 2017). Further, climate models have shown that melt ponds contribute not only to the heat and mass balances of sea ice, but also play a role in how much ice remains at the end of summer (Flocco et al., 2010; Flocco et al., 2012; Hunke et al., 2013). In fact, studies have found that the timing of spring melt pond development may be important for predicting how much sea ice remains at the end of summer (Schröder et al., 2014; Liu et al., 2015).

Given the importance of melt ponds in the Arctic climate system and the spectral differences between snow-covered sea ice, bare ice and melt ponds, efforts have gone into producing pan-Arctic melt pond products from optical satellite systems. Rösel et al. (2012) utilized the Moderate Resolution Imaging Spectroradiometer (MODIS) 8-day atmospherically corrected surface reflectance product together with a spectral unmixing algorithm to produce an 8-day based melt pond fraction data set for 2000–2011. In a different approach, Lee et al. (2020) applied machine learning approaches to top-of-the-atmosphere (TOA) MODIS reflectances, together with normalized band differences from four MODIS visible and near-infrared bands. This approach minimized the impact of anisotropic reflectance and atmospheric correction effects that exist when using MODIS atmospherically corrected data, which are not optimized for sea ice regions. Multi-layer neural networks and multinomial logistic regressions were used to retrieve melt pond fraction and binary melt pond vs. ice classification between May and August from 2000 to present. Zege et al. (2015) used another approach and a different satellite source: based on the physical and optical characteristics of sea ice and melt ponds without a priori information, an iterative process using the Newton-Raphson method was applied to Medium

* Corresponding author at: Industrial Environment Cell, Research Institute of Industrial Science and Technology (RIST), Pohang 37673, South Korea.
E-mail address: sglee7619@gmail.com (S. Lee).

https://doi.org/10.1016/j.rse.2023.113920
Received 13 January 2023; Received in revised form 9 November 2023; Accepted 17 November 2023
Available online 30 November 2023

Table 1
Summary of three melt pond products.

	Sensor	Time span	Type	Algorithm	Main input (i.e., band)	Spatial resolution of main input (m)	Gridded resolution (km)	Temporal resolution
R2012	MODIS	8 May to 13 Sep. 2002–2012	Fraction	Neural networks	Band 1, 2, and 3	500	12.5	8-day
Z2015	MERIS	1 June to 30 Sep. 2002 1 May to 30 Sep. 2003–2011	Fraction	Iterative Newton-Rhapson method	1, 2, 3, 8, 10, 12, 13, and 14	1000	12.5	Daily
L2020	MODIS	1 May to 31 Aug. 2000-Present	Fraction/ Binary	Multi-layers neural networks and logistic regression	Normalized band differences among band1–4	250 and 500	5.0	Daily

Table 2
Modification of temporal resolution of melt pond products.

	Day (i.e., 8-day)	Month
W1	9–16 May	
W2	17–24 May	Proxy of May
W3	25 May −1 June	
W4	2–9 June	
W5	10–17 June	Proxy of June
W6	18–25 June	
W7	26 June - 3 July	
W8	4–11 July	
W9	12–19 July	Proxy of July
W10	20–27 July	
W11	28 July – 4 August	
W12	5–12 August	Proxy of August
W13	13–20 August	
W14	21 – 28 August	

Table 3
Monthly mean ratio of first-year ice, Multi-year ice, and Ambiguous classes over sea ice in May to August 2005–2011.

	First-year ice (%)	Multi-year ice (%)	Ambiguous (%)
May	74	11	15
June	64	4	32
July	63	1	36
August	51	13	36

Resolution Imaging Spectrometer (MERIS) reflectance data. An atmospheric and bi-directional reflectance distribution function (BRDF) was applied to correct for the anisotropic reflectance properties of sea ice and melt ponds. Although each algorithm aims to retrieve melt ponds using optical satellite data, melt pond fractions differ based on the input data used as well as the methods employed. Further, temporal resolution differs between these three data sets (i.e. daily, 8-day or monthly). It is likely that each melt pond product has its own advantages and disadvantages, but a full assessment of how they compare has yet to be done.

Here, we intercompare the above-mentioned melt pond products from 2002 to 2011. Clear-sky high resolution optical imagery from Worldview (WV) and Landsat are used as a baseline assessment of accuracy. Melt pond classifications derived from Planet SkySat and helicopter imagery during the Multidisciplinary drifting Observatory for the Arctic Climate (MOSAiC) campaign are used as well for comparison. We further evaluate how well the satellite-retrieved melt pond fractions correspond to surface albedo and depend on sea ice type.

A comparative analysis of the different melt pond products can provide a recommendation to the science community regarding which products are suitable for their different needs.

2. Data & methods

2.1. Melt pond products

This study evaluates three publicly available melt pond products over the 2002–2011 period that all three products are available (see Table 1). Melt pond fraction is defined as the fractional area of ponded ice within the satellite pixel. The first data product is the Rösel et al. (2012) (hereafter R2012) approach, which expanded on Tschudi et al. (2008)'s earlier work that utilized atmospherically corrected MODIS data (i.e., MOD09A1; https://lpdaac.usgs.gov/products/mod09a1v006/) together with spectral unmixing. To speed up the processing for a large volume of MODIS data, an Artificial Neural Network (ANN) approach was implemented. A disadvantage of the method, however, is that the atmospheric correction that goes into the MOD09 product is not optimized for the polar regions (i.e., unknown amounts of aerosol optical depth, water vapor and ozone). Another issue is that the Bidirectional Reflectance Distribution Function (BRDF) of snow/sea ice and melt ponds are not explicitly accounted for in this data set. Melt ponds and bare sea ice scatter light anisotropically, such that the assumption of a Lambertian surface can lead to unrealistic results during melt (e.g., Zege et al., 2015, hereafter Z2015). Both of these issues are problematic when training the algorithm with spectral reflectance data obtained in situ, which are integrated over the entire hemisphere and taken under specific atmospheric conditions. The R2012 melt pond data set is available as 8-day composites on a 12.5 km spatial resolution polar stereographic grid.

The second data set (Z2015) produces melt pond fractions and spectral sea ice albedo from MERIS Level 1B optical imagery. An analytical iterative procedure based on the Newton-Raphson method without *a prior* information on the sea ice spectral albedo was applied, which explicitly accounts for atmospheric correction and the BRDF of sea ice surfaces. When information on atmospheric variables, such as aerosol optical depth are not available, default models that represent background Arctic conditions are used. These data are available at daily temporal resolution and are also gridded to a 12.5-km spatial resolution polar stereographic projection.

Finally, Lee et al. (2020) (hereafter L2020) worked with calibrated Level 1B TOA 250 and 500 m MODIS reflectances (e.g. MOD02HKM, https://ladsweb.modaps.eosdis.nasa.gov/missions-and-measurements/products/MOD02HKM). To reduce biases from incorrect atmospheric correction assumptions, and to minimize the BRDF effect, normalized band ratios were used as input into machine learning algorithms. As such the approach is not dependent on in situ data to train the algorithm. Melt pond fraction and binary melt pond classification were retrieved by multinomial logistic regression and multi-layer neural networks, respectively. Furthermore, since the departure from a Lambertian surface for ice and snow surfaces increases at high solar (θ_o) and viewing (θ_v) zenith angles, pixels corresponding to $\theta_o > 70^\circ$ and $\theta_v > 50^\circ$ were

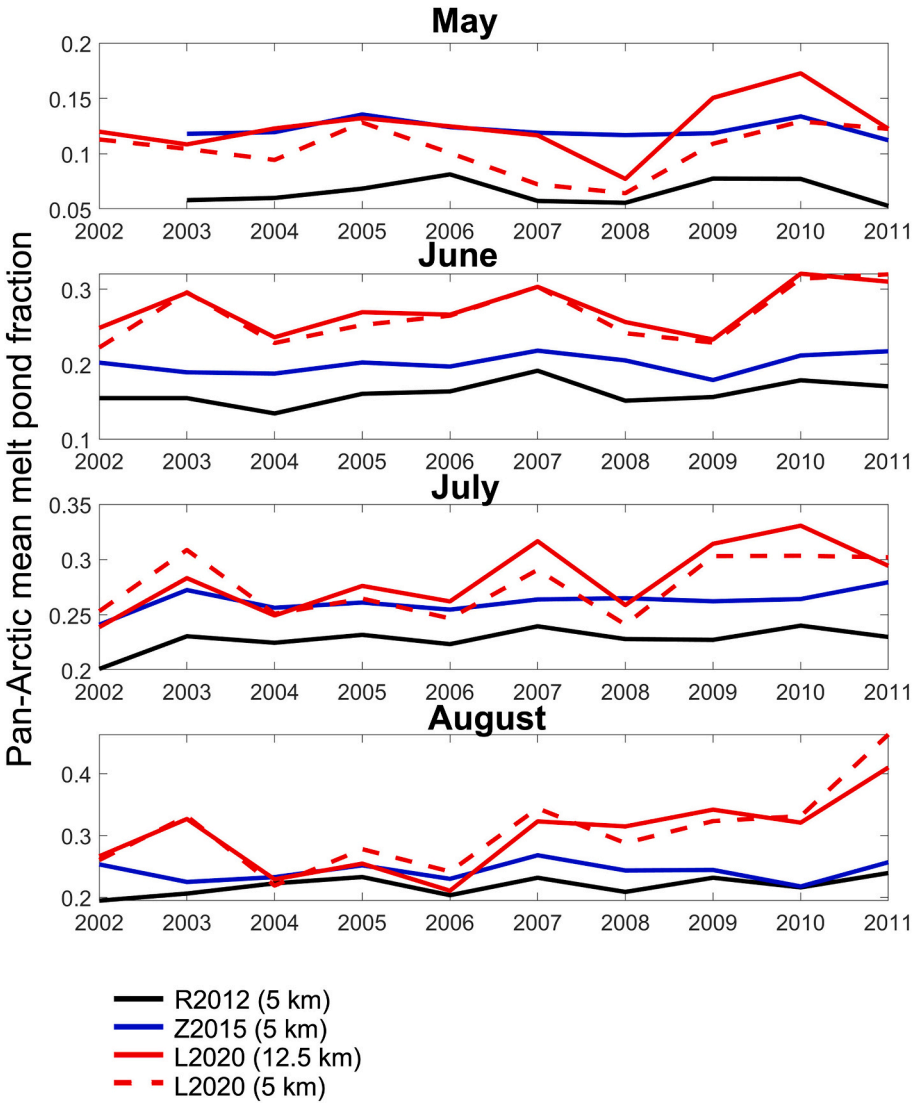

Fig. 1. Time-series of Pan-Arctic monthly mean melt pond fractions for each data set from 2002 to 2011. Results from L2020 are given at two spatial resolutions, 5 km (dashed line) and 12.5 km (solid line). Note the different y-axis scales across panels.

Table 4
Correlation coefficients between total melt pond fractions as averaged over the entire Arctic Ocean for each summer month from 2002 to 2011 (confidence interval: 95%).

Correlation coefficients	May	June	July	August
R2012 vs. Z2015	0.62	0.73	0.72	0.44
R2012 vs. L2020	0.40	0.71	0.46	0.54
Z2015 vs. L2020	0.54	0.69	0.61	0.35

excluded. Finally, in order to avoid "false" melt pond identification once ponds are refrozen, surface temperatures from the MOD29 (1-km Ice Surface Temperature (IST)) product were used to eliminate refrozen melt ponds in August. Refer to Lee et al. (2020) for further information. While melt pond classification is based on daily 500 m TOA reflectances, the spatial resolution of the resulting melt pond product is subsequently degraded to 5 km for the full time-series (2000−2023). Melt ponds are produced as daily and monthly averages and are provided on the Equal-Area Scalable Earth (EASE)-grid.

As R2012 does not provide daily melt pond estimates, daily melt ponds from Z2015 and L2020 are merged into 8-day melt pond composites (weeks evaluated are listed in Table 2). We further composite these into monthly means for long-term melt pond change analysis among the three data products. To intercompare seasonal and interannual variability among these data sets, all data sets are regridded to a 12.5-km EASE-grid using nearest neighbor interpolation. When comparing against higher resolution data (e.g. WorldView and Landsat), the native resolution of each product is used. Since each product has a different pole hole area, the largest pole hole (from Z2015) is applied to all products for time series comparison (Table 3 and Fig. 1). Note, the difference in the location of the sea ice edge among the three products is <3%. When generating monthly averaged melt pond fractions it is important to note that cloud cover will influence the number of days that go into the monthly average. In both the daily Z2015 and L2020 data sets, the number of days and hence overall satellite pixels used to create the monthly averaged pan-Arctic melt pond fraction in a given month varies with cloud fraction. The mean daily cloud cover fractions over sea ice areas (defined using a 15% sea ice concentration threshold) in the Z2015 data set are 44, 37, 60 and 58% in May, June, July and August, respectively, while those for L2020 in the same months are 77, 66, 78%, and 84%. Both products typically exhibit higher cloud fraction in July and August than in May and June (Taylor et al., 2019).

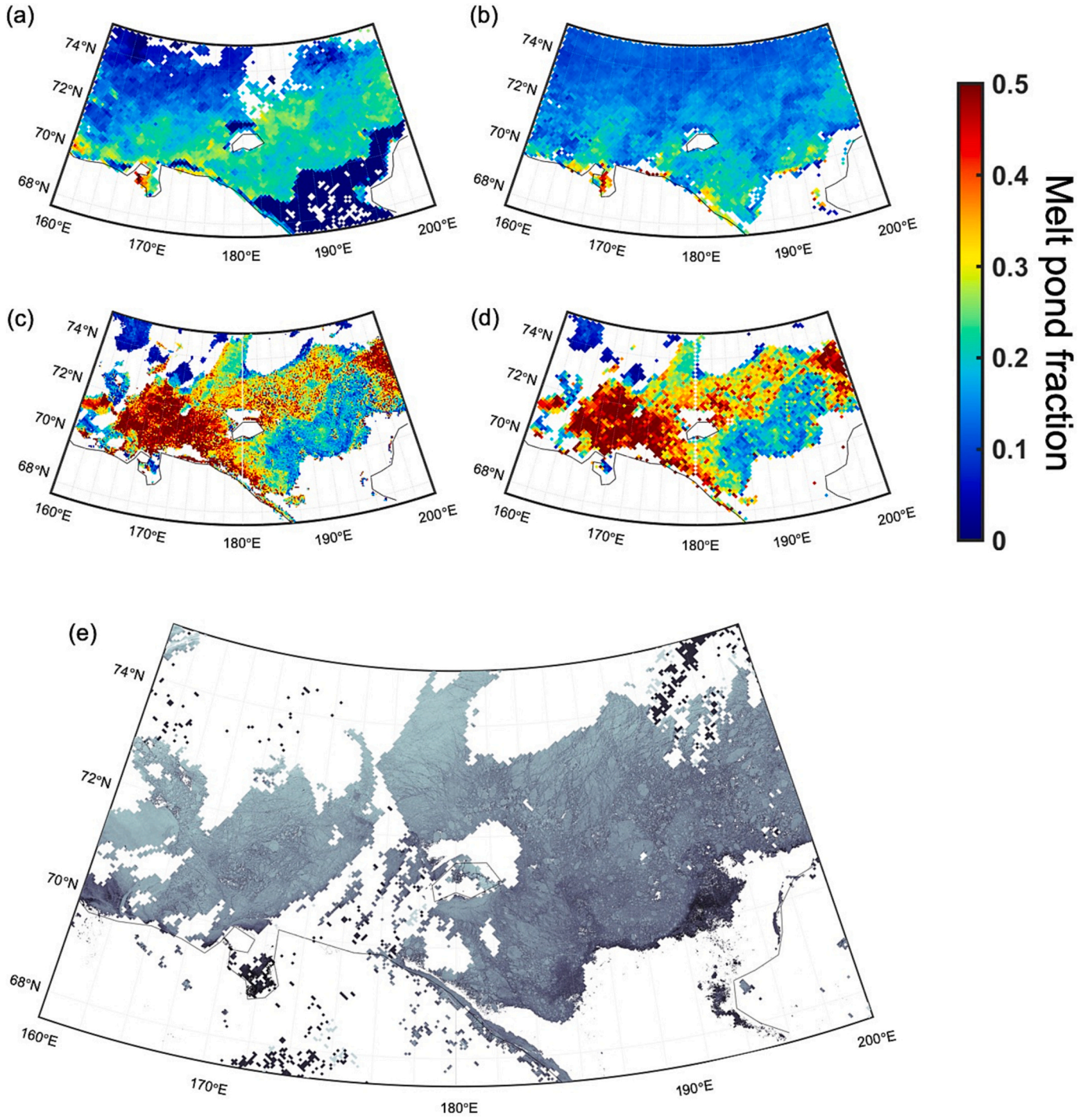

Fig. 2. 8-day composited (2–9 June 2003) melt pond fractions from (a) R2012, (b) Z2015, (c) L2020 at 5-km spatial resolution and (d) L2020 at 12.5-km spatial resolution. An Aqua MODIS RGB 250-m scene from 6 June 2003 is shown in (e). The blank areas represent cloud covers and ocean areas. (For interpretation of the references to colour in this figure legend, the reader is referred to the web version of this article.)

2.2. Higher resolution data

We compare the coarser resolution melt pond datasets against those retrieved from five classified 2 m DigitalGlobe's WorldView imagery (hereafter WV), as well as one Landsat-5 image (hereafter Landsat). Melt pond classification derived from WV follows the approach of Wright and Polashenski (2018) who developed an open-source algorithm to automatically classify four sea ice surface types from WV panchromatic and 8-band multispectral data: snow/thick ice, dark/thin ice (i.e., it is not snow covered, and can include nilas and young ice during freeze-up), melt ponds/submerged ice, and ocean. While snow/thick ice, dark/thin ice are combined into one ice class, melt ponds/submerged ice is classified as melt ponds. After classifying the WV images, the classes are converted to pond fraction following Lee et al. (2020). While more WV images would have been desirable, it is challenging to find WV scenes that are cloud-free and spatially and temporally coincident with the three melt pond products. As melt pond fractions from R2012 are only provided as 8-day composites, we may not expect the composite to match exactly with the location/date of the WV image. On the other hand, while melt ponds from Z2015 are from the same date, the

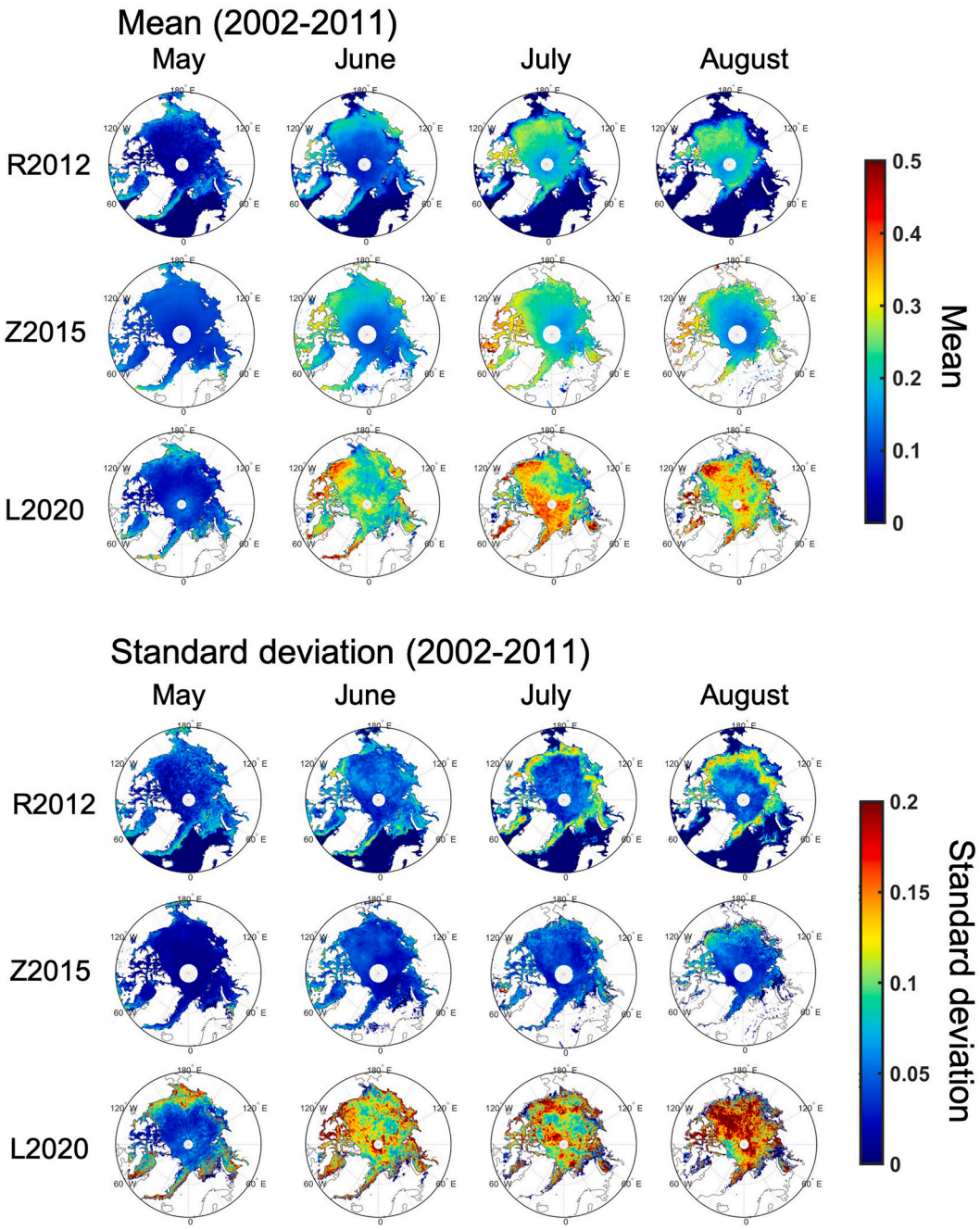

Fig. 3. Mean and standard deviation of melt pond fractions averaged from 2002 to 2011 for May through August from each dataset.

acquisition time is unknown. For L2020, we were able to locate WV images that were within 20 h of the MODIS swath (see Table 4).

Since Landsat has a larger swath than WV and a spatial resolution of ~30 m, this comparison has the benefit of including a larger area than can be achieved using WV data. The disadvantage is that there is no melt pond classification algorithm currently available for Landsat. Nevertheless, the data are useful for a visual assessment of melt pond locations. One Landsat image from 11 July 2008 is utilized here.

Finally, we additionally include melt pond classifications around the MOSAiC drifting station. The melt pond classification results are obtained using Planet SkySat satellite and helicopter imagery with a spatial resolution of 0.5 m and between 0.03 and 0.5 m, respectively. (Wright et al., 2021; Niels, 2023). The SkySat imagery does not provide RGB composite imagery. The classification algorithm for SkySat used is same as the one employed for WV classification (Wright and Polashenski, 2018). The three-band (RGB) helicopter images are available as classified orthomosaics (Fuchs and Birnbaum, 2023). Surface type classes including melt ponds were derived with the customized classification tool PASTA-ice (Fuchs, 2023). It is notable that these data come from marginal ice zone in Fram Strait characterized by high sea ice dynamics, fragmentation, and the flooding at the edge of ice.

2.3. Albedo and sea ice type data

Surface albedo and sea ice type were additionally utilized to assess their relationship with the pan-Arctic retrieved melt pond fractions. Clear-sky surface albedo comes from the National Oceanic and Atmospheric Administration (NOAA) Climate Data Record (CDR) of Extended and Advanced Very High Resolution Radiometer (AVHRR) Polar Pathfinder (APP-x; Key et al., 2016). The APP-x set contains several visible-

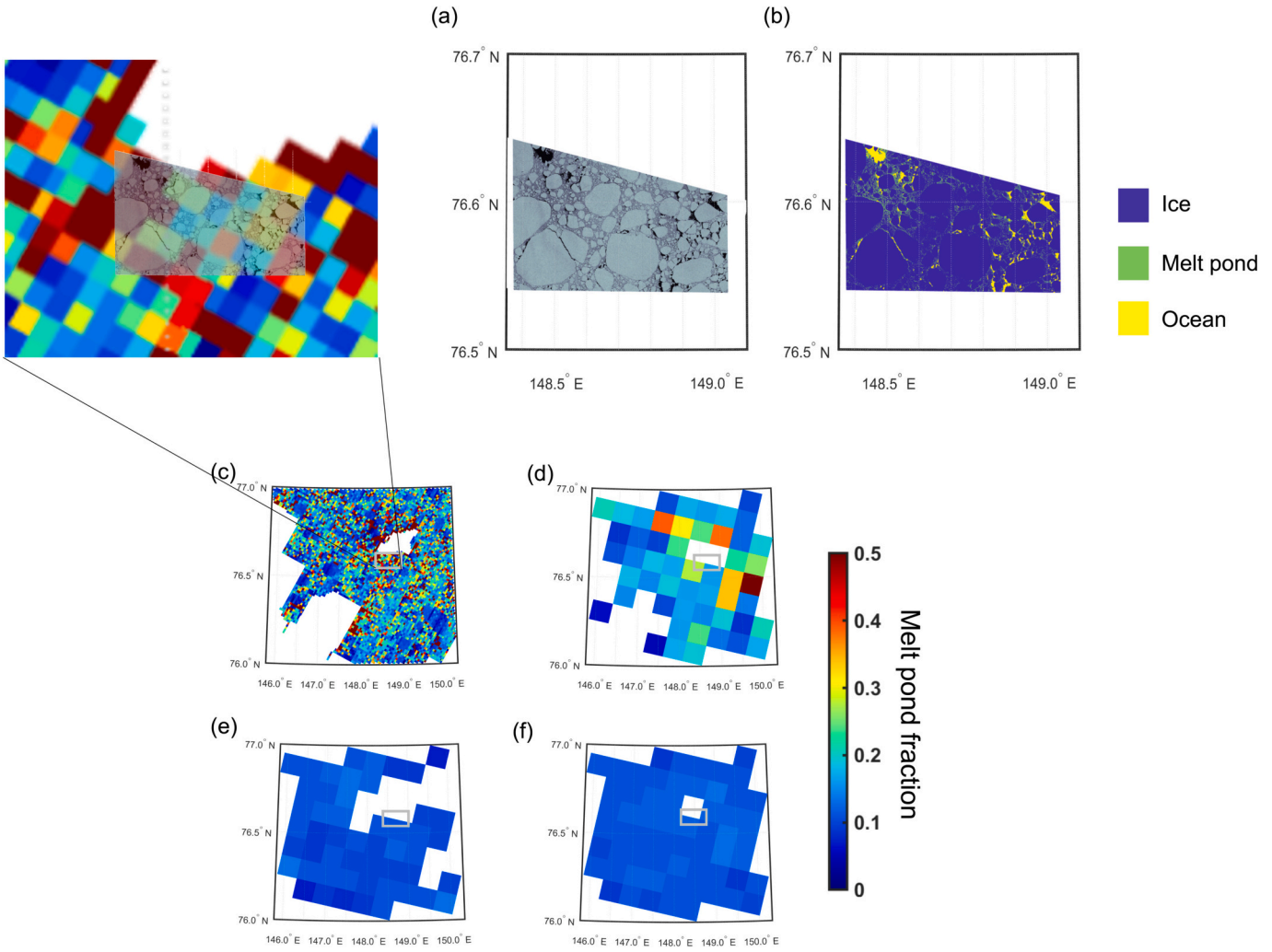

Fig. 4. (a) WV band 2 (i.e., blue band) on 14 June 2010. (b) WV classification results on 14 June 2010 (Wright and Polashenski, 2018). (c) melt pond fraction from L2020 with the native resolution (i.e., 500 m) on 14 June 2010. (d) melt pond fraction from L2020 gridded into 12.5 km on 14 June 2010. (e) melt pond fraction from R2012 8-days composite centered on 10–17 June 2010. (f) melt pond fraction from Z2015 on 14 June 2010. (For interpretation of the references to colour in this figure legend, the reader is referred to the web version of this article.)

and thermal-infrared-retrieved geophysical variables from 1982 to present. These data are available twice daily (0400 and 1400 local solar time) at 25-km spatial resolution. Here we use the afternoon pass (1400).

Sea ice type is derived from multi-sensor inputs, including Special Sensor Microwave-Imager/Sounder (SSMIS), AMSR2, and ASCAT, through the Ocean and Sea ice Satellite Application Facility (OSI SAF) (Aaboe et al., 2021). The three ice type classes are first-year ice (FYI), multi-year ice (MYI), and ambiguous. During summer, microwave emission and backscatter is impacted by liquid water, resulting in more pixels classified as ambiguous. This is problematic then in evaluating the role of ice type on melt pond fractions. Table 3 shows monthly mean ratio of FYI, MYI, and ambiguous classes. In particular, the ratio of ambiguous class is >30% in June and August 2005 to 2011. When the ratio of ambiguous classes is >50% over sea ice (defined using a 15% sea ice concentration threshold), it is not used in comparison with melt pond fraction. The ambiguous class is also excluded for the comparison. Sea ice type data is available daily from 2005 to present at 10 km spatial resolution.

In our comparisons below we create monthly averages of surface albedo and ice type, regrid them to 12.5 km and compare against the 12.5 km gridded monthly melt pond fractions. Spatial correlations between albedo and pond fractions are provided for May to August over the 2002 to 2011 time-period.

3. Results

Below we start with an intercomparison of the long-term monthly melt pond fractions from each data set at 12.5-km spatial resolution before comparing the products against higher spatial resolution data.

3.1. Intercomparison of melt pond fraction

Time-series of pan-Arctic averaged monthly melt pond fractions from 2002 to 2011 for May through August are shown in Fig. 1. All three products generally show similar interannual variability in pan-Arctic melt pond fractions, though the agreement varies between months, with higher agreement generally in June and July and worse agreement at the start and end of the melt season (e.g., May and August) (Table 4). For example, a high correlation ($r \geq 0.62$) is found between R2012 and Z2015 in all months except for August when it drops to $r = 0.44$. Overall, despite Z2015 having the least amount of interannual variability, it is the most highly correlated product with R2012. The highest correlation with L2020 occurs in June, on the order of $r = 0.70$ for both R2012 and Z2015, whereas in May and August the correlations decrease to 0.54 or less. Good agreement between L2020 and Z2015 is also found in July (r

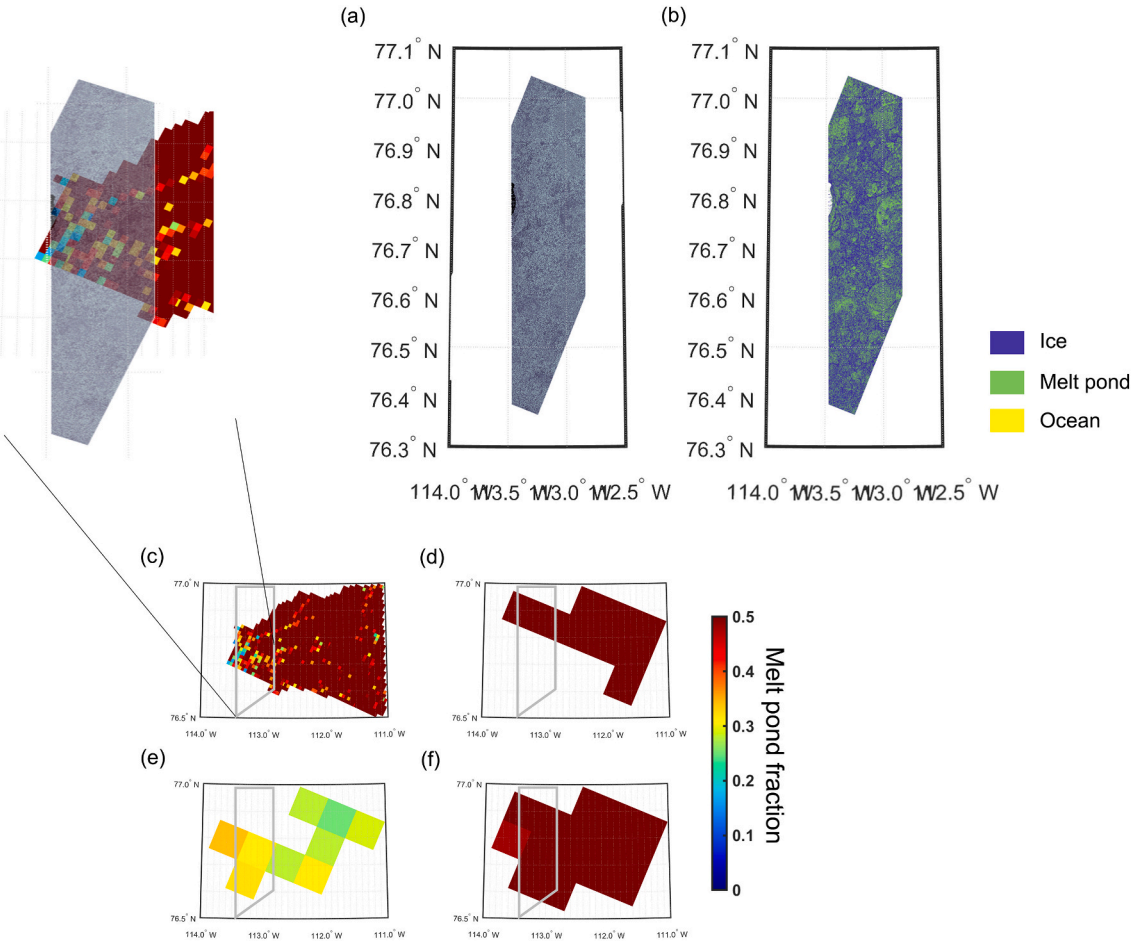

Fig. 5. (a) WV band 2 (i.e., blue band) on 25 June 2010. (b) WV classification results on 25 June 2010 (Wright and Polashenski, 2018). (c) melt pond fraction from L2020 with the native resolution (i.e., 500 m) on 25 June 2010. (d) melt pond fraction from L2020 gridded into 12.5 km on 25 June 2010. (e) melt pond fraction from R2012 8-days composite centered on 18–25 June 2010. (f) melt pond fraction from Z2015 on 25 June 2010. (For interpretation of the references to colour in this figure legend, the reader is referred to the web version of this article.)

= *0.61*), but not with R2012.

In terms of long-term trends, the different retrieval methods mostly do not indicate a trend in pond fractions between 2002 and 2011. The exception is in July when mean fraction slightly increases (largest in the L2020 algorithm). L2020 further indicates an increase in melt pond fraction also in August. This increase starts in 2006, and the highest August melt pond fraction occurred in 2011, exceeding 40% of the sea ice area. The positive trends in July and August are not statistically significant.

Despite similar interannual variability, the areal coverage of melt ponds can differ considerably between data sets. Since L2020 relies on normalized band ratios between the blue and near-infrared bands, there is increased sensitivity to liquid water (Lee et al., 2020). This may falsely lead to wet snow being classified as a melt pond. The use of these two bands may also result in cases of thin ice and leads/cracks to be classified as melt ponds. Combined, this may help to explain why L2020 has considerably higher pond fractions in June compared to the other data sets as this is the time of year when melt onset starts over large parts of the Arctic Ocean (e.g. Stroeve et al., 2014). Interestingly, none of the data sets show monthly mean melt pond fractions in excess of 35% during the peak of the melt season in July in contrast to earlier studies (e.g., Romanov, 1995; Tschudi et al., 2008; Perovich et al., 2007). One reason could be that these studies provided melt pond fractions at higher spatial resolution resulting in overall higher percentage of ice area covered by ponds. However, regridding the L2020 data from 5 km to 12.5 km results in slightly higher melt pond fractions between May and July. It is only in August that the coarser resolution data resulted in lower pond fractions, and only between 2005 and 2007. Thus, melt pond fractions retrieved at different spatial scales may not be directly comparable.

In general, R2012 has the lowest melt pond fraction in most months, while the L2020 product has the overall highest melt pond fractions. May is an exception, when sometimes the Z2015 algorithm gives the largest overall pond fractions in several years. Confirmation of a positive bias in L2020 melt pond fractions in May 2009 and 2010 is seen through visual inspection of the level-2250-m and 500-m spatial resolution MODIS images (not shown). Leads and cracks between ice floes are easily identifiable at 500 m, and while they should be separately classified as open water, it appears those are often falsely classified as melt ponds, especially within the marginal ice zone (MIZ). Since the L2020 melt pond algorithm is first run on the 500-m data before spatial averaging to 5 km, variability in leads/cracks from year-to-year may in part also explain the higher interannual variability seen in the L2020 data set. Monthly spatial melt pond fractions from all data sets are shown in the supplementary material from 2002 to 2011 (Fig. S1).

One curious deviation between products occurs later in the time-series when melt pond fractions from L2020 start to increase faster than the other data products. For example, starting in July 2009, there is a spike in melt pond fraction as a result of high pond fractions within the Chukchi and Beaufort seas (see Fig. S1) that continues in subsequent years. Similarly, in August 2007 there is a step-wise increase in pond fraction. One would expect an increase in melt pond fraction during

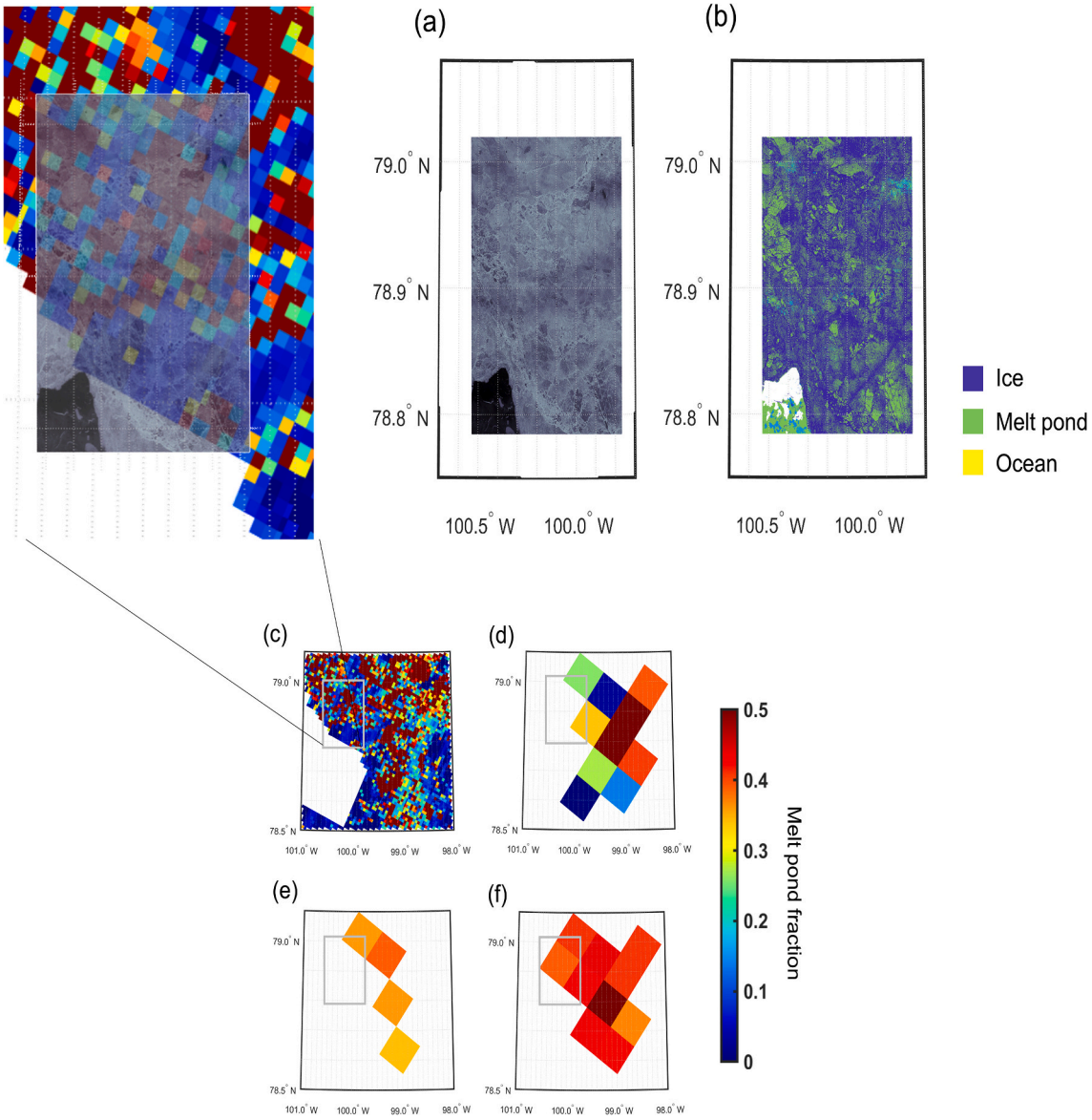

Fig. 6. (a) WV band 2 (i.e., blue band) on 3 July 2010. (b) WV classification results on 3 July 2010 (Wright and Polashenski, 2018). (C) melt pond fraction from L2020 with the native resolution (i.e., 500 m) on 3 July 2010. (d) melt pond fraction from L2020 gridded into 12.5 km on 3 July 2010. (e) melt pond fraction from R2012 8-days composite centered on 26 June ~3 July 2010. (f) melt pond fraction from Z2015 on 3 July 2010. (For interpretation of the references to colour in this figure legend, the reader is referred to the web version of this article.)

August given the delays in freeze-up across most of the Arctic (e.g. Stroeve and Notz, 2018). Trends in freeze-up from 2002 to 2011 are on the order of 1 to 4 days yr^{-1} each year, yet there is a discernable shift in later freeze-up in 2007 that could explain the observed increase in pond fraction.

Further insights behind the seasonal differences are revealed by looking at differences in the spatial patterns. Fig. 2 shows an example of an 8-day composite in early June (2–9 June 2003) together with an Aqua MODIS RGB 250-m image (6 June 2003). R2012 and Z2015 retrieve low melt pond fractions in the East Siberian Sea, whereas L2020 exhibits pond fractions exceeding 50% in many areas. The corresponding RGB MODIS image shows either very thin or flooded level ice by melt water in this region. Note that here and throughout the paper, we use the term "flooding" to describe sea ice that is inundated by meltwater, rather than the flooding that is associated with negative freeboard and snow-ice formation. In regions of level first-year ice, the surface often becomes extensively covered by melt ponds rather than forming smaller, isolated ponds like those typically observed on multiyear sea ice. In some instances, extensive ponding over level sea ice can be difficult to discern from very thin ice. This highlights the challenges of visually identifying what constitutes a melt pond. While melt ponds are not easily identifiable in the MODIS image, given the time of year of this image and the fact that the melt onset already began (spatially averaged melt onset date of 7 May), it is probable that there could be thin ice and/or flooding of the level ice by melt water that is then picked up as melt pond fraction using L2020.

To further highlight spatial variability between the data sets, we show the mean 2002–2011 averaged melt pond fractions for each month together with the standard deviation in Fig. 3. On average, the 2002–2011 mean spatial patterns in melt pond fraction are broadly similar in May, but this changes dramatically as the summer progresses. Despite some similarities in spatial patterns as to where melt ponds tend to be more extensive (i.e., the Beaufort, Chukchi, and East Siberian seas in June), the magnitudes differ substantially, especially in comparison to the L2020 data set. The L2020 product suggests melt ponds expand north of Greenland in July and across the Arctic Ocean in August,

Table 5
WV mean melt pond fraction and mean melt pond fraction of three melt pond products. When the pond fraction is in red, it most closely matches the WV classification.

WV date and time (hh:mm)	Time difference with L2020 MODIS	Image acquisition location	WV mean melt pond fraction based on the classification (%)	Mean melt pond fraction from L2020 500 m in the grey box (%)	Mean melt pond fraction from L2020 12.5 km in the grey box (%)	Mean melt pond fraction from R2012 in the grey box (%)	Mean melt pond fraction from Z2015 in the grey box (%)	RMSE between L2020 500 m and WV in the grey box	RMSE between L2020 12.5 km and WV in the grey box	RMSE between R2012 12 5 km and WV in the grey box	RMSE between Z2015 12.5 km and WV in the grey box
14 June 2010 00:40	4 h 30 mins	East Siberian Sea	9.3	35.2	30.7	11.2	12.6	24.2	22.3	3.1	4.4
25 June 2010 15:25	3 h 40 mins	Arctic Archipelago	42.9	51.2	45.3	32.7	54.7	6.5	3.4	10.5	12.2
3 July 2010 03:50	20 h	Arctic Archipelago	33.6	33.7	30.5	36.7	38.6	1.3	2.7	3.5	6.5
4 May 2011 12:00	2 h 15 mins	North Ellesmere island	8.0	13.7	11.2	0.3	4.7	4.7	2.5	7.9	4.2
13 July 2011 22:25	30 mins	Chukchi Sea	36.9	34.2	32.8	24.5	28.7	2.8	3.7	11.2	7.8
20 June 2022 13:32	9 mins	Barents Sea	15.4	26.2	24.1	–	–	11.9	8.6		
20 July 2022 08:53	33 mins	Kara Sea	7	10.2	11.9	–	–	3.9	4.2		

reaching fractions as high as 50%, whereas the other two products show modest melt pond coverage in these regions during advanced melt. Leads and small open water area detected by the MODIS 500 m scale around MYI zone and central Arctic in July and August, leading to high L2020 melt pond fraction. High melt pond fractions near the pole in August have been observed during field campaigns, including during the year-long Multidisciplinary drifting Observatory for the Study of Arctic Climate (MOSAiC) expedition (e.g. see Fig. 1, Stroeve et al., 2022).

In all products, the standard deviation is smallest in May, with interannual variability limited to the MIZ, where melt first begins and there is high temporal variability in the timing of melt onset. However, as summer progresses, the standard deviation increases over a larger region. Regions with a high standard deviation are generally limited to the MIZ in R2012 and Z2015, but slightly expand to more northerly locations by August. Overall, Z2015 shows the least amount of interannual variability (seen also in Fig. 1), with Arctic-averaged standard deviations from May to August of 0.03, 0.05, 0.05, and 0.04, respectively. L2020, on the other hand, shows the largest and most widespread standard deviations which peak in August. Large interannual variability is not surprising in August as this is the time of year when melt pond fractions start to refreeze and thus melt pond fraction is strongly dependent on synoptic weather patterns that vary from year-to-year. The larger standard deviation in L2020 agrees with the larger interannual variability seen in Fig. 1 and the step-wise increase in melt pond fraction in recent years.

3.2. Comparison against high-resolution images (i.e., Worldview and Landsat)

It is challenging to fully assess why the three products sometimes provide very different melt pond fraction estimates since they use (1) different sensors, (2) different inputs from those sensors, (3) different approaches for masking out clouds, (4) different techniques of compositing, and (5) data with different spatial resolutions. Nevertheless, to assess the reliability of the different products, we compare melt pond fractions in 2010 and 2011 against high-resolution melt pond fractions derived from WV and imagery from Landsat.

We first focus on comparisons against those retrieved from WV imagery using the Wright and Polashenski (2018) classification algorithm. The WV image on 14 June 2010 shows large ice floes surrounded by thin or brash ice, with few melt ponds and small open water areas between the floes (Fig. 4(a) and (b)) The WV melt pond fraction in this scene is 9.3% (Table 4). Pond fractions from R2012 (10–17 June 2010) and Z2015 are in close agreement with the WV melt pond classification, showing few melt ponds in the vicinity of the WV image and an overall pond fraction below 12% over the larger area. On the other hand, both the 500-m and the 12.5-km spatial resolution L2020 data set produces relatively high melt pond fractions within the WV scene (35.2% and 30.7%, respectively). In this instance, it appears that the thin ice areas are classified as melt ponds by L2020. Later in the melt season (25 June and 3 July 2010), WV imagery near Ellesmere Island show higher melt pond fractions (Figs. 5 and 6), and all three melt pond products estimate broadly similar pond fractions that agree with the WV classification. Overall, L2020 matches best with the WV data on both these dates, with the lowest RMSE value (see Table 5).

Another early melt season example (4 May 2011) demonstrates the L2020 algorithm outperforming R2012 and Z2015. Interestingly, while this WV scene is quite early in the melt season given the northerly location (i.e., North of Ellesmere Island), the WV classification suggests 8% of the scene contains melt ponds (Fig. 7 and Table 5). R2012 and Z2015 significantly underestimate the melt pond fraction, with fractions on the order of 0.3% and 4.7%, respectively. The temporal-resolution differences with the WV image may be one explanation for the low bias in R2012 and Z2015. On the other hand, movement of sea ice is limited in this region, so the temporal mismatch may not be the only factor. By 13 July 2011, all three data products show more advanced melt pond formation in agreement with the WV imagery (Fig. 8). The L2020 data product once again gives the highest melt pond fraction at 34.2% and is close to the WV value of 36.9%, while R2012 and Z2015 give pond fractions of 24.5% and 28.7%, respectively (Table 5 and Fig. 8).

For comparison with WV in 2022, only L2020 data are available. The melt pond fraction derived from L2020 was found to be higher than the WV-based melt pond fraction (Figs. 9 and 10). While the image

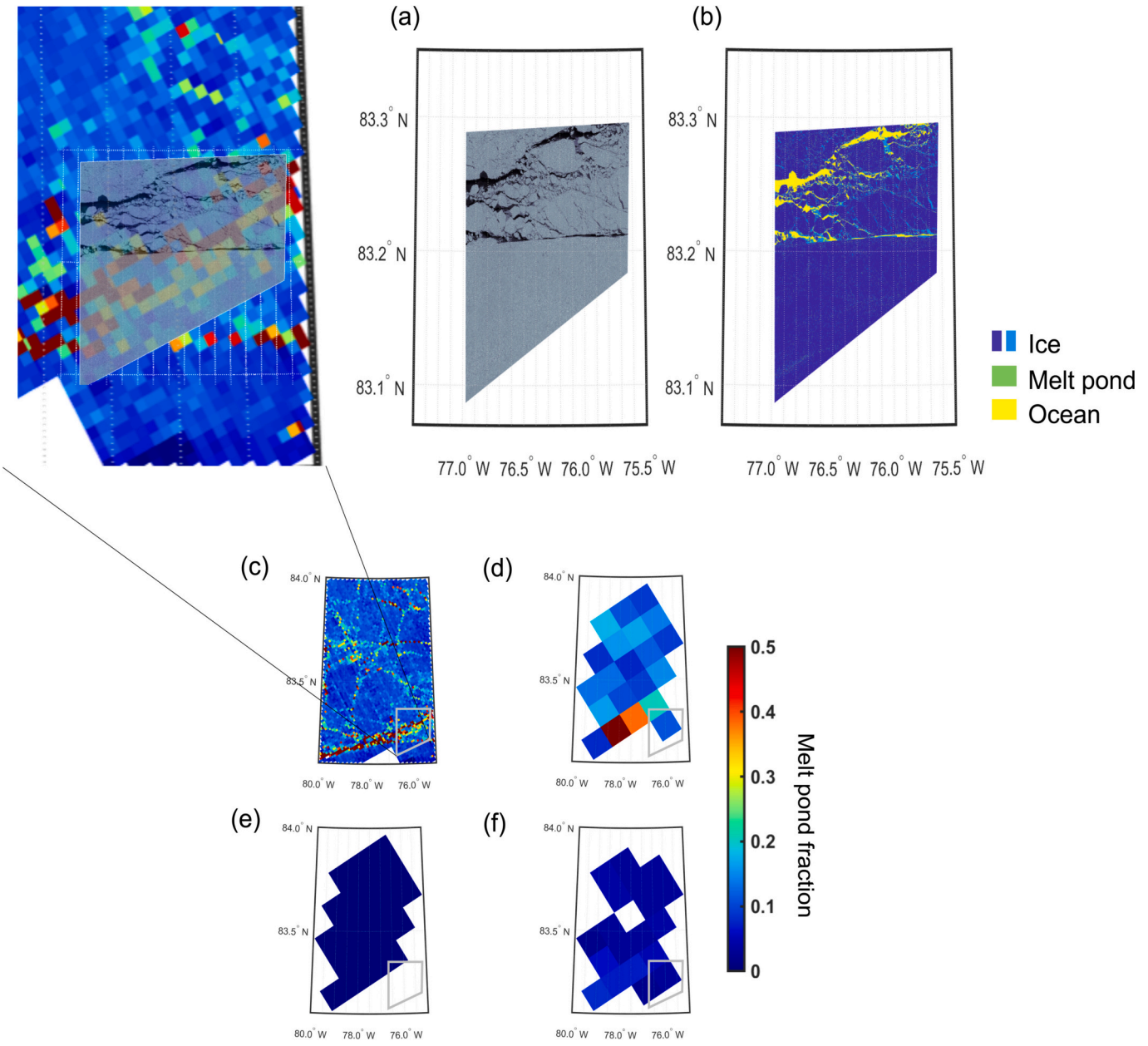

Fig. 7. (a) WV band 2 (i.e., blue band) on 4 May 2011. (b) WV classification results on 4 May 2011 (Wright and Polashenski, 2018). (c) melt pond fraction from L2020 with the native resolution (i.e., 500 m) on 4 May 2011. (d) melt pond fraction from L2020 gridded into 12.5 km on 4 May 2011. (e) melt pond fraction from R2012 8-days composite centered on 9–16 May 2011. (f) melt pond fraction from Z2015 on 4 May 2011. (For interpretation of the references to colour in this figure legend, the reader is referred to the web version of this article.)

acquisition times on 20 June and 20 July are only 9 and 33 min apart, respectively, a slight spatial mismatch may have led to the higher overall detected melt ponds in the L2020 data product, as some of the open water areas seen in the two data sets are not perfectly aligned. It is also apparent that the WV classification algorithm mis-classified some open water areas in the lower left-hand corner as melt ponds on 20 July 2022.

Overall, based on the few WV comparisons performed, the R2012 agreed best with the WV data on 14 June 2010 and underestimated the pond fractions on the other dates. Outside of 14 June 2010, L2020 provided the best agreement with WV-classified images.

We also examined a Landsat scene within the MIZ in Beaufort Sea on 11 July 2008. This scene was within 21 min of a corresponding MODIS swath. Within this scene, L2020 once again indicates the highest melt pond fractions, followed by Z2015, and then R2012 (Fig. 11). The Landsat image shows clear evidence of surface flooding in the lower center part of the image where high melt pond fractions are retrieved using L2020. However, these comparisons come with an important caveat as the ice is moving and thus an exact spatial match is not possible. This is especially problematic within the MIZ where the ice can be highly dynamic, and especially for comparisons with the R2012 algorithm as it only provides 8-day composites.

Finally, we also include a comparison of melt pond classifications for the MOSAiC expedition with the melt pond fraction obtained from L2020 on 22 June 2020 (SkySat) and 22 July 2020 (helicopter-borne melt pond) (Fig. 12 and Fig. 13). The temporal difference between L2020 and Skysat/Helicopter-borne image is 28 mins and 1 h 22 mins,

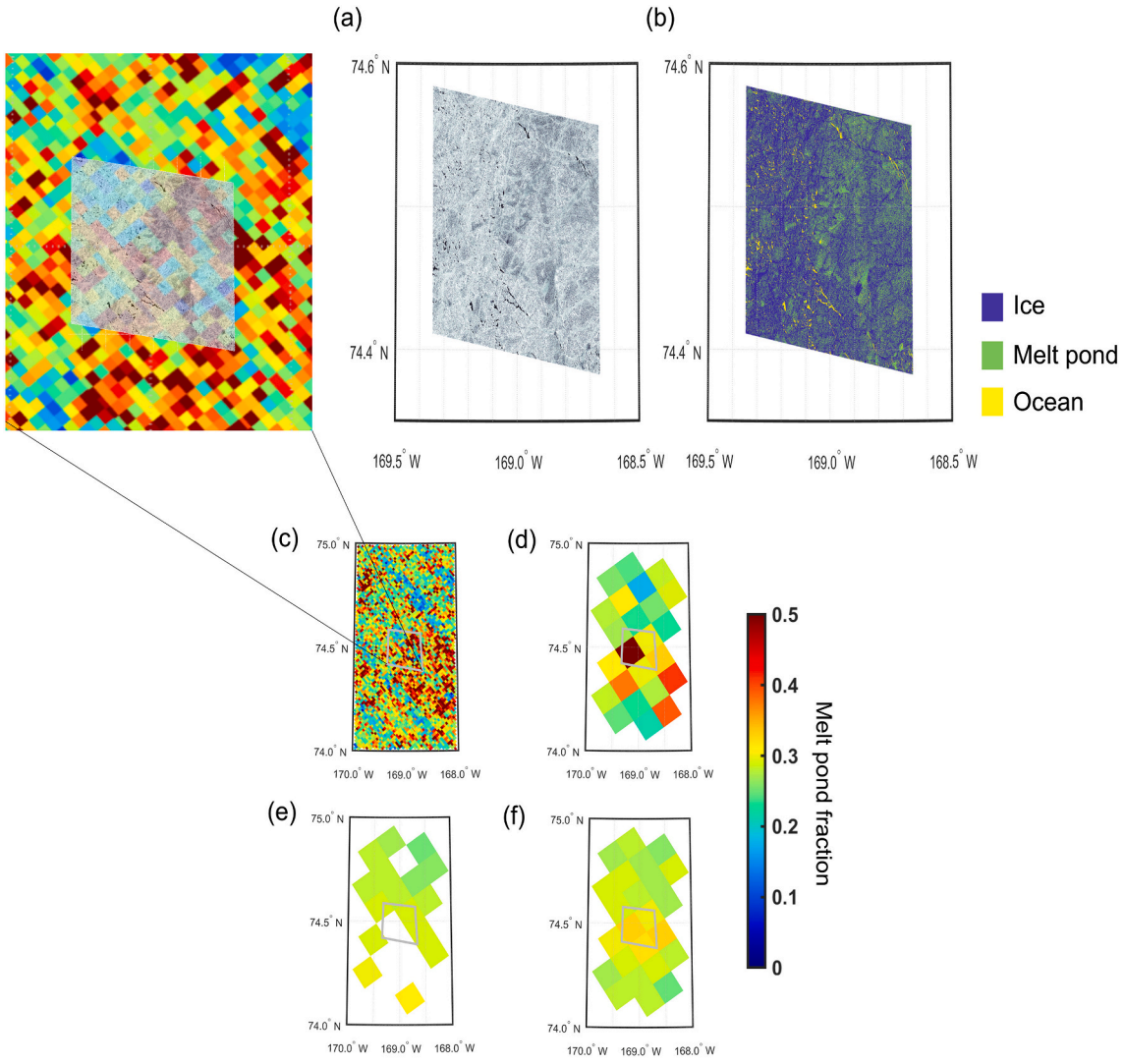

Fig. 8. (a) WV band 2 (i.e., blue band) on 13 July 2011. (b) WV classification results on 13 July 2011 (Wright and Polashenski, 2018). (c) melt pond fraction from L2020 with the native resolution (i.e., 500 m) on 13 July 2011. (d) melt pond fraction from L2020 gridded into 12.5 km on 13 July 2011. (e) melt pond fraction from R2012 8-days composite centered on 12–19 July 2011. (f) melt pond fraction from Z2015 on 13 July 2011. (For interpretation of the references to colour in this figure legend, the reader is referred to the web version of this article.)

respectively. The L2020 melt pond fraction on 22 June 2020 with a spatial resolution of 500 m and 12.5 km is found to be 15.2% and 14.7%, respectively. In contrast, the melt pond fraction derived from SkySat is found to be 10.1%. This pond fraction is somewhat low for the time of year, yet the MOSAiC floe was located above 81°N and thus we could expect lower overall melt pond fractions. In this comparison, the swath width of the SkySat image is less than for WV and thus the 12.5-km data product only had two pixels within the scene In terms of comparison against helicopter-borne melt pond classification, considering the time of year and temporal difference between the helicopter-borne image and L2020, the fraction difference between helicopter-borne image (24.5%) and L2020 (53.3%) is 28.8%.

Overall, it is not surprising that L2020 tends to outperform the other two data sets in many of these intercomparisons given the data product is produced at a higher spatial resolution. As one would expect, the coarser the melt pond fraction data set (i.e., 12.5 km), the less the product can capture the spatial heterogeneity of the sea ice surface. Thus, higher-resolution products may be in better agreement with one another. On the other hand, L2020 tends to estimate a higher melt pond fraction compared to the other two data products especially early in the melt season in part because leads and small open water areas are sometimes misclassified as melt ponds. The L2020 algorithm also tends to map flooded level ice as melt ponds. While this perhaps is not exactly a melt pond in the classic sense, flooded ice will have similar impacts on the energy balance and light penetration through the ice. Thus, depending on the application of the melt pond datasets, this information may still be useful.

However, it is also important to note that differences in acquisition times can also lead to biases in the comparison for the other data products, especially during periods of fast ice drift. This is challenging to correct for as current ice motion data products are not of sufficient spatial and temporal resolutions to capture drift speed a few hours apart. Thus, an accuracy assessment of the R2012 and Z2015 is more challenging to assess. While these inter-comparisons cannot conclusively point to which melt pond product best captures the “true” melt pond fraction, they do provide a general sense of performance and the

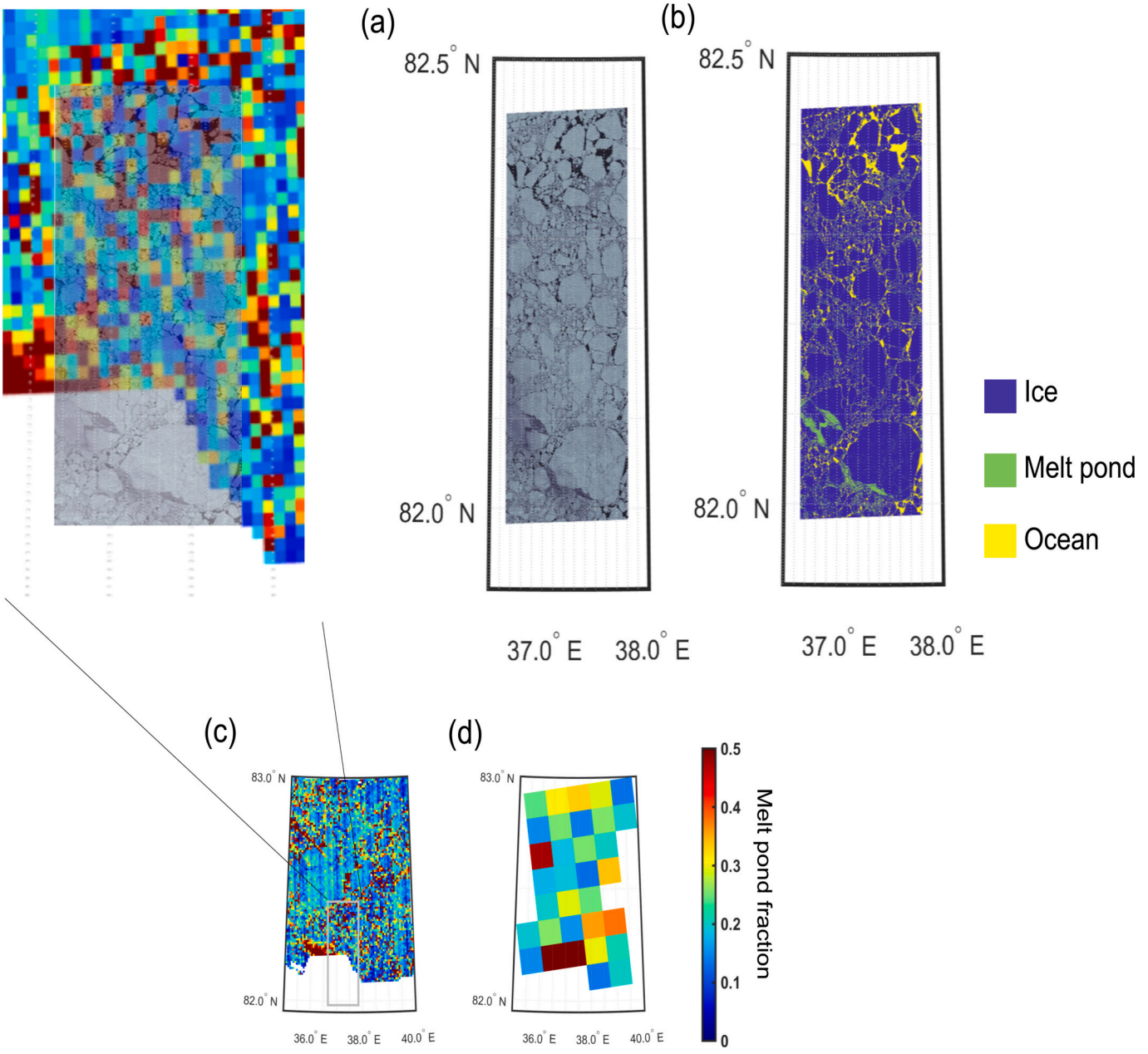

Fig. 9. (a) WV band 2 (i.e., blue band) on 20 June 2022. (b) WV classification results on 20 June 2022 (Wright and Polashenski, 2018). (c) melt pond fraction from L2020 with the native resolution (i.e., 500 m) on 20 June 2022. (d) melt pond fraction from L2020 gridded into 12.5 km on 20 June 2022. (For interpretation of the references to colour in this figure legend, the reader is referred to the web version of this article.)

difficulties in mapping melt ponds at the relatively coarse spatial resolution of MODIS or MERIS data.

3.3. Comparisons against albedo and sea ice type

We lastly evaluate the relationship between interannual pond fractions, surface albedo and sea ice type. The surface albedo gradually decreases over time as melt ponds develop (Polashenski et al., 2012; Perovich and Polashenski, 2012), but even before melt ponds develop the albedo drops as the snow melts (Curry et al., 1995). By mid-July most snow has melted except near thicker, deformed ice where snow drifts can persist. The APP-X minimum surface albedo of 0.1 to 0.4 in July coincides with peak melt pond fraction, while in August, drained or refrozen melt ponds cause the albedo to increase towards the bare sea ice value of 0.7 (Light et al., 2022).

As expected, a negative correlation exists between melt pond fraction and surface albedo (Fig. 14). Z2015 pond fractions are highly correlated with surface albedo across most of the Arctic Ocean ($R < -0.70$) (Fig. 14b) whereas high correlations ($R = -0.65$) for R2012 are limited to the north of Greenland and the Canadian Arctic Archipelago (Fig. 14a). L2020 pond fractions are overall weaker correlated with surface albedo throughout the entire Arctic region ($-0.83 < R < -0.3$).

Times-series of monthly melt pond fraction and albedo from May to August for a location north of Greenland (85.383°N, 17.475°W) is

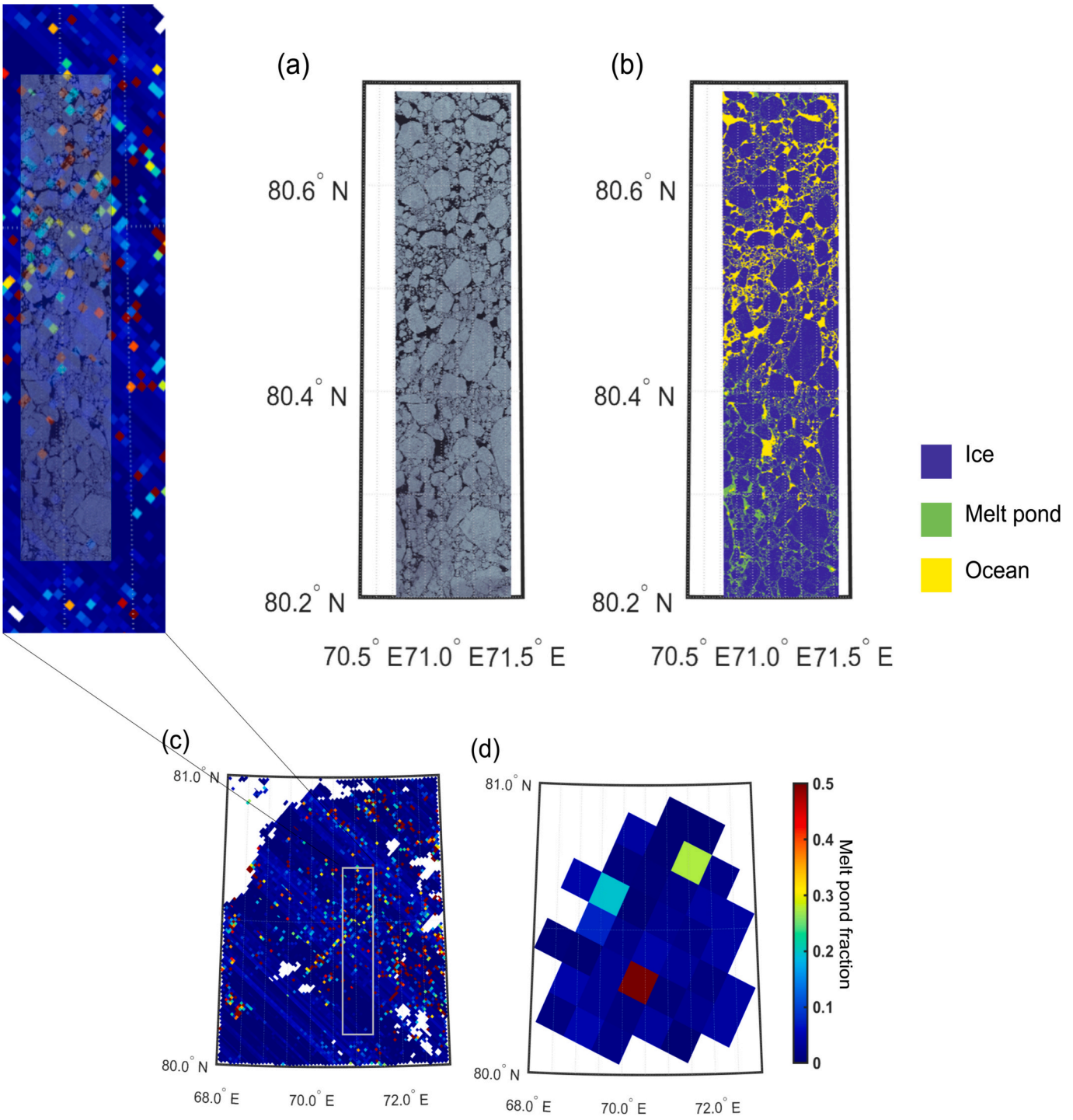

Fig. 10. (a) WV band 2 (i.e., blue band) on 10 July 2022. (b) WV classification results on 10 July 2022 (Wright and Polashenski, 2018). (c) melt pond fraction from L2020 with the native resolution (i.e., 500 m) on 10 July 2022. (d) melt pond fraction from L2020 gridded into 12.5 km on 10 July 2022. (For interpretation of the references to colour in this figure legend, the reader is referred to the web version of this article.)

shown in Fig. 14d. In general, the surface albedo decreases from May to July and somewhat increases in August, whereas melt pond fraction increases from May to July and then slightly declines in August, leading to inverse correlation coefficients of −0.72 (R2012), −0.80 (Z2015), and − 0.40 (L2020). However, sometimes melt pond fractions decline despite the albedo decreasing. For example, between May and June in 2002, 2006, and 2009, the L2020 melt pond fractions decrease. A decrease in R2012 melt pond fraction from May to June is also seen in 2009. A decrease in melt pond fraction can occur by rapid melt water drainage (Polashenski et al., 2012; Perovich and Polashenski, 2012; Tanaka, 2020), which is normally reflected by an increase in the surface albedo. Another reason could be a result of excessive cloud coverage that biases both the monthly melt pond estimate as well as the clear-sky albedo. For example, since L2020 employs a strict cloud screening process, the monthly mean for June 2008 is based on just three days (28–30 June). The lack of sufficient clear-sky days also occurs in July 2004 (only three clear-sky days).

Using the sea ice type masks, we find that melt pond fraction on FYI

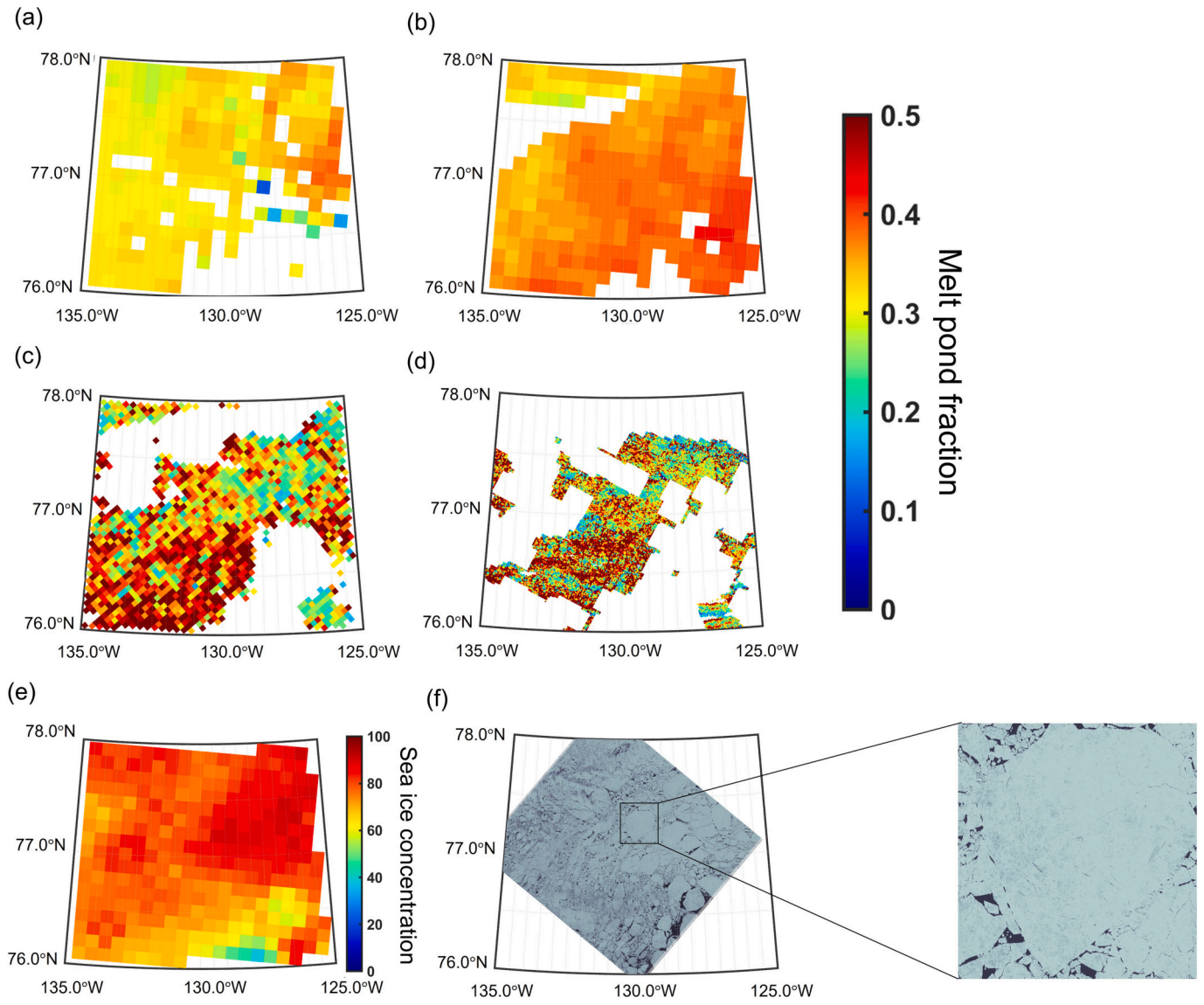

Fig. 11. (a) melt pond fraction from R2012, 8-days composite centered on 4–11 July 2008; (b) melt pond fraction from Z2015 on 11 July 2008; melt pond fraction from L2020 on 11 July 2008 at (c) 5 km spatial resolution and (d) 500 m swath data. The black areas in (a)-(d) are regions classified as clouds. (e) sea ice concentration from AMSR-E on 11 July 2008. (f) Landsat-5 band 1(i.e., blue band) on 11 July 2008.

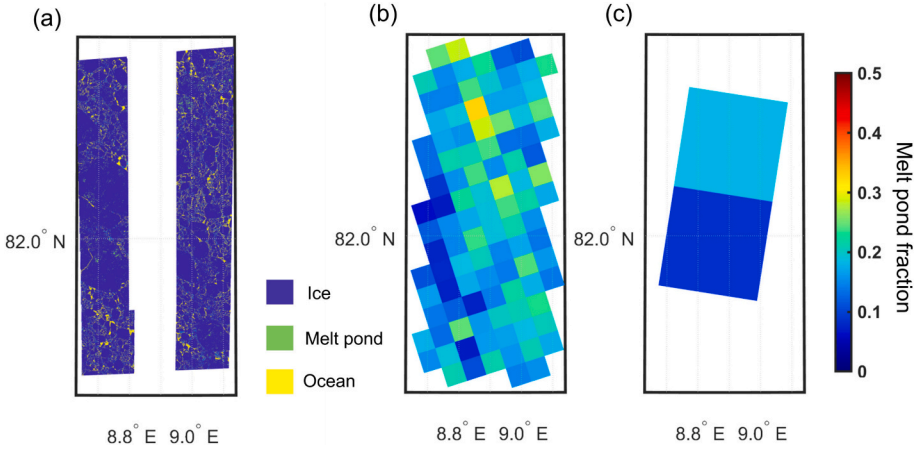

Fig. 12. (a) Melt pond classification derived by Skysat from MOSAiC expedition. (b) melt pond fraction from L2020 with the native resolution (i.e., 500 m) on 22 June 2020. (c) melt pond fraction from L2020 gridded to 12.5 km on 22 June 2020. The time difference between Skysat and MODIS is 28 mins.

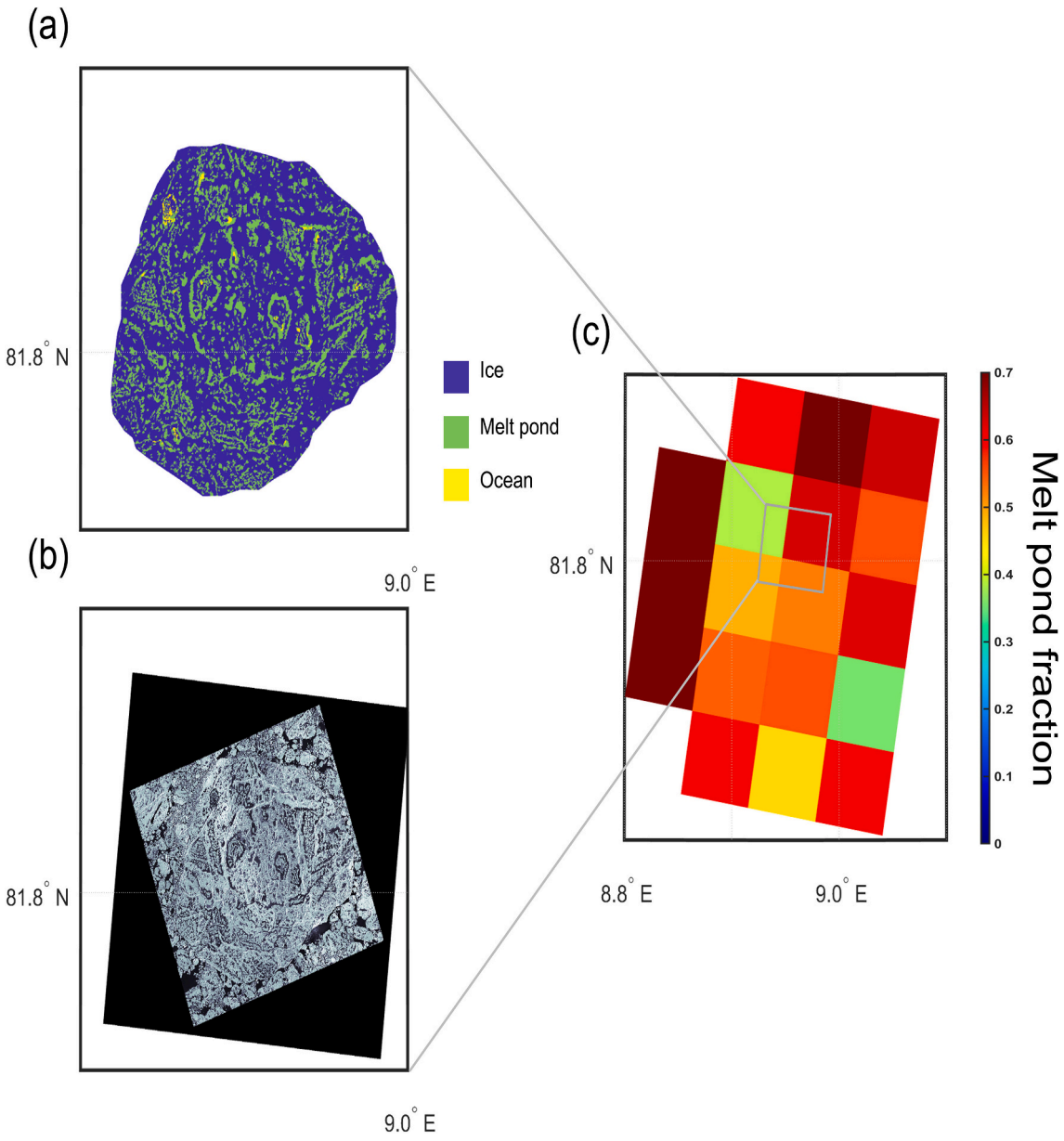

Fig. 13. (a) Melt pond classification of the MOSAiC Central Observatory 2 floe (expedition leg 4) (b) blue band derived by helicopter from MOSAiC expedition. (c) melt pond fraction from L2020 with the native resolution (i.e., 500 m) on 22 July 2020. (For interpretation of the references to colour in this figure legend, the reader is referred to the web version of this article.)

is typically higher than that on MYI. An exception is noted in May 2007 and 2009. The small open water areas classified as FYI in the East Siberian Sea in May 2007, where L2020 estimates high melt pond fraction (Sup. Fig. 1). Z2015 produces lower pond fractions around the Beaufort Sea, which is classified as MYI, resulting in lower fraction in May 2009 than June (Sup. Fig. 1).

From May to August, the daily mean differences in Z2015 melt pond fractions between FYI and MYI are 2%, 5%, 4%, and 3%. On the other hand, the corresponding differences in L2020 melt pond fractions are 2%, 6%, 13%, and 17%. The melt pond fraction on FYI shows greater variability than on MYI. L2020 displays larger deviations within every month than Z2015. While melt pond fraction from Z2015 and L2020 on FYI is larger than on MYI in June, Webster et al (2015) demonstrates melt pond fraction on MYI surpasses on FYI in June around the Chukchi Sea (Fig. 15).

Since monthly averages exclude the spatio-temporal variability that is important for initiating melt pond formation, we show examples of regionally averaged melt pond fractions together with albedo in Fig. 16. The NSIDC regional mask (https://nsidc.org/data/g02186/versions/1) is used for calculating regional averages for eight Arctic Ocean regions. Since the R2012 dataset is not available at daily resolution, it is not included.

While there is an inverse relationship between melt pond fraction and albedo across all regions, the level of co-variation between the two variables differs across regions. The daily melt pond evolution from L2020 shows more temporal variability than Z2015, which tends to

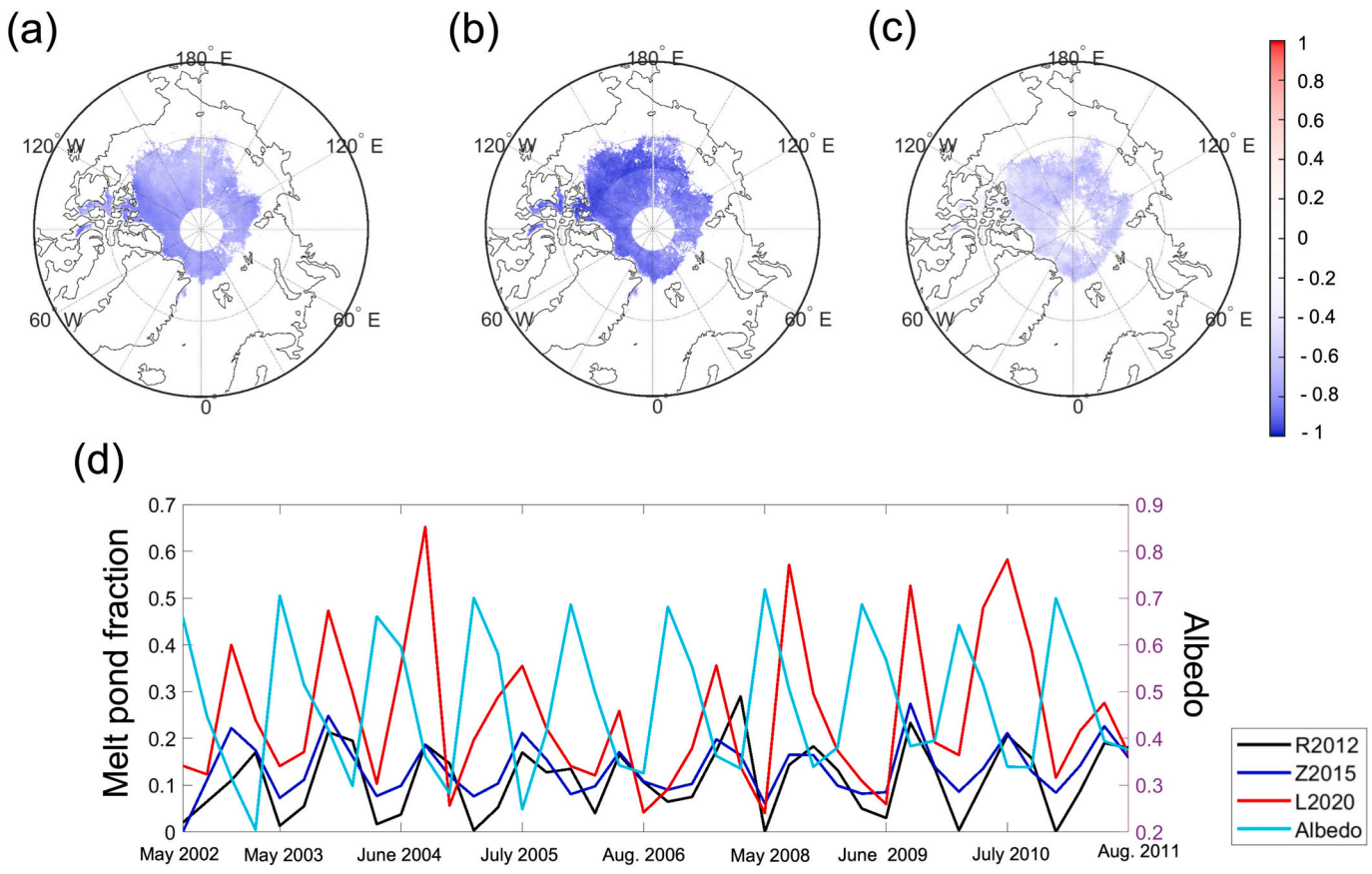

Fig. 14. The correlation map between melt pond fraction and albedo from May to August from 2002 to 2011. (a) R2012 vs. albedo, (b) Z2015 vs. albedo, (c) L2020 vs. albedo, (d) the time series of R2012, Z2015, L2020, and albedo at North Greenland (85.383°N, 17.475°W).

gradually increase through July and then decrease in August. L2020 generally shows similar increases and decreases yet is considerably noisier. While the albedo rapidly decreases after early to mid-June, the albedo exhibits little temporal variability.

Next we analyzed the spatial distribution of melt ponds in comparison with albedo over landfast ice in the East Siberian Sea. Note however that the spatial distribution of melt pond fractions from each product can differ due to the different cloud screening processes involved in data product (Figs. 17 and 18). While the monthly mean melt pond fraction from L2020 is generally higher than that from R2012 and Z2015, the mean melt pond fraction from L2020 is lower in East Siberian Sea on 13 July 2003 (Fig. 17). The intercomparison results on 17 June 2010 are similar to those on 13 July 2003 (Fig. 18). Although the overall melt pond fraction spatial distributions are similar, at 72°N/132°E, the L2020 produces noticeably lower fractions than R2012, and in a region where the surface albedo is around 0.35.

4. Discussion

While we cannot clearly state which melt pond product is most accurate based on the above comparisons, some general statements can be made about how the products differ. This information may help users make informed decisions about which product is most suitable depending on the application as well as provide insights as to how the data providers may improve their products. This study demonstrates that MODIS and MERIS-derived melt pond products suffer from a loss of detail as compared to high-resolution imagery like WV, Landsat, and Skysat. While the spatial resolution of input data for the melt pond data products evaluated is <1-km, it is worth noting that the gridded resolution of L2020 is nearly twice as high as that of R2012 and Z2015. Thus, it is not surprising that L2020 better matches the higher resolution melt pond estimates. On the other hand, since sea ice is dynamic, direct matching of WV or Landsat with a MODIS or MERIS image complicates these intercomparisons. It is further difficult to find clear-sky coincident higher resolution images, limiting the number of intercomparisons used in this study. We also cannot fully assess whether the satellite-based melt pond products are higher or lower than in-situ observations (Webster et al 2022). To further address the accuracy of the individual data sets, a comprehensive field campaign that combines in situ data, airborne imaging, high resolution (< 3 m) and coarse resolution (<12.5 km) satellite data is needed.

Coarse resolution satellite data is the only way to observe the pan-Arctic daily. Despite the limitations of the three satellite data products evaluated, the seasonal evolution is broadly consistent between the data sets. The key differences pertain to pond fractions in June and August, when the L2020 data product consistently shows higher pond fractions as well as higher interannual variability. It appears L2020 is more sensitive to ice flooding, thin ice and leads, which may lead to an overestimation of melt pond fraction. On the other hand, it is unclear if flooded ice should not also be classified as a melt pond. While L2020 produced higher melt pond fractions than R2020 and Z2015, in comparison with WV, melt pond fractions from L2020 in closer agreement to those derived from WV imagery. The spatial distribution of L2020 is more correlated than Z2015 in the spatial comparison with other melt related variables. Although the dependence on using a normalized band ratio between the blue and the near-infrared band may result in more

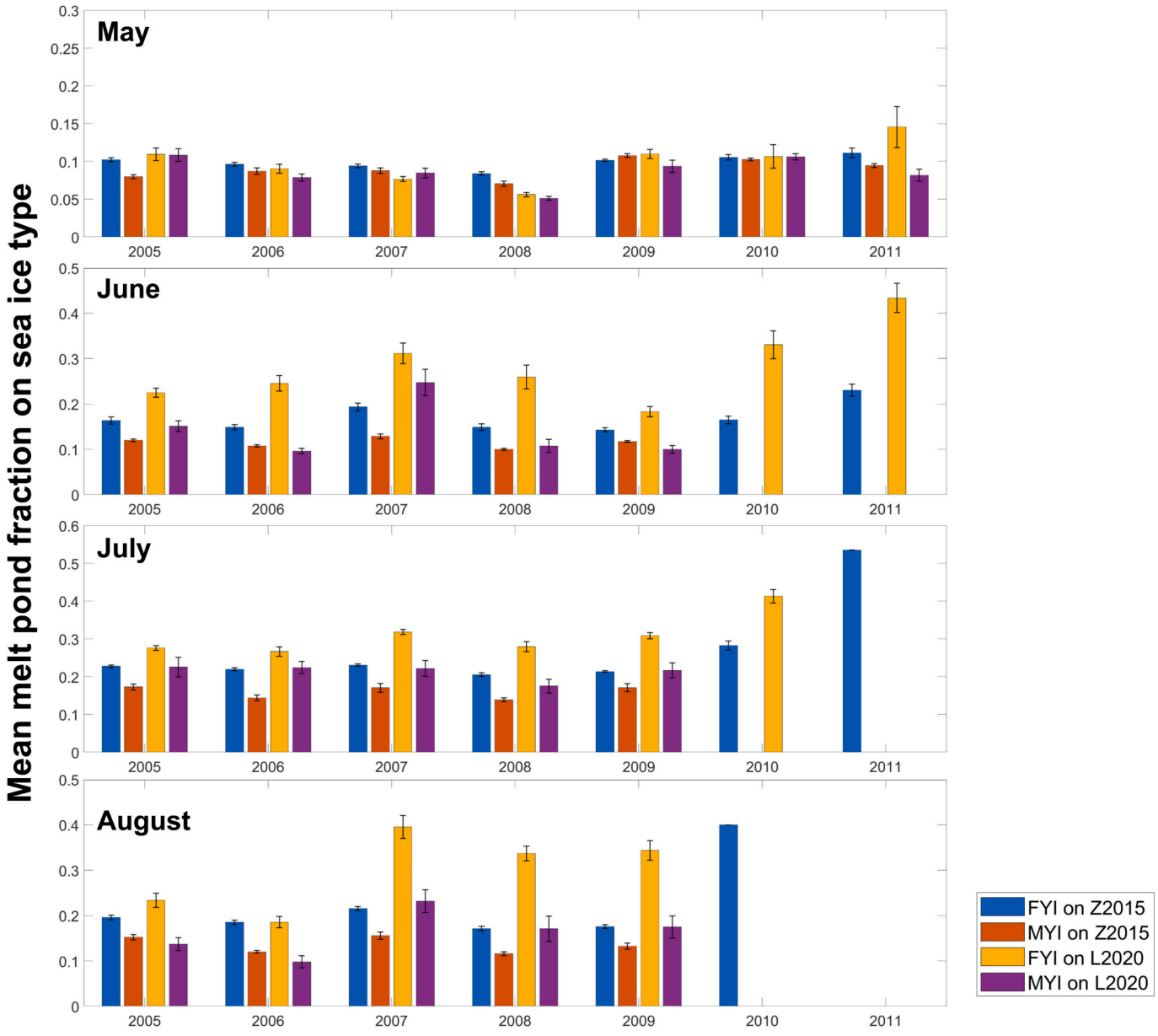

Fig. 15. Mean melt pond fraction based on sea ice type (i.e., FYI and MYI) from 2005 to 2011.

sensitivity to liquid water in the L2020 data product, the use of band ratios helps to reduce biases from incorrect atmospheric correction assumptions and minimizes errors related to unknown BRDF distributions. While L2020 melt pond fractions in August are larger than the other data products despite the removal of refrozen melt ponds from the final pond fraction estimates, this is in agreement with trends towards later freeze-up.

It is interesting that none of the data sets show monthly mean melt pond fractions in excess of 35% during the peak of the melt season in July in contrast to earlier studies (e.g., Romanov, 1995; Tschudi et al., 2001; Perovich et al., 2002). These studies provided melt pond fractions at higher spatial resolution than those used here and thus a direct comparison may not be validA path forward could be to blend melt pond classification results from WV with those from MODIS/MERIS to obtain increased spatial structure and improved information on melt pond characteristics. L2020 melt pond fraction shows good agreement with WV-based classification results, yet its monthly correlation with albedo is weaker than R2012 and Z2015. This is because km-scale albedo cannot explain change in albedo by the spatial detail of melt pond.

Finally, it is unclear how best to classify flooded ice. Flooded ice is common over level ice, such as first-year or landfast ice. For example, in Dease Strait (Nunavut) one study found that as a result of delayed melt pond formation, >95% of the level ice was flooded on the 18th of June 2014 (Diaz et al., 2018). This extensive flooding had to do with level ice that was covered by 10 cm of new snow prior to a period of warm air temperatures.

5. Conclusions

Given the importance melt ponds play in the Arctic climate system, pan-Arctic melt pond products have historically been a critical data gap. Several studies have tried to fill this data gap by developing satellite-

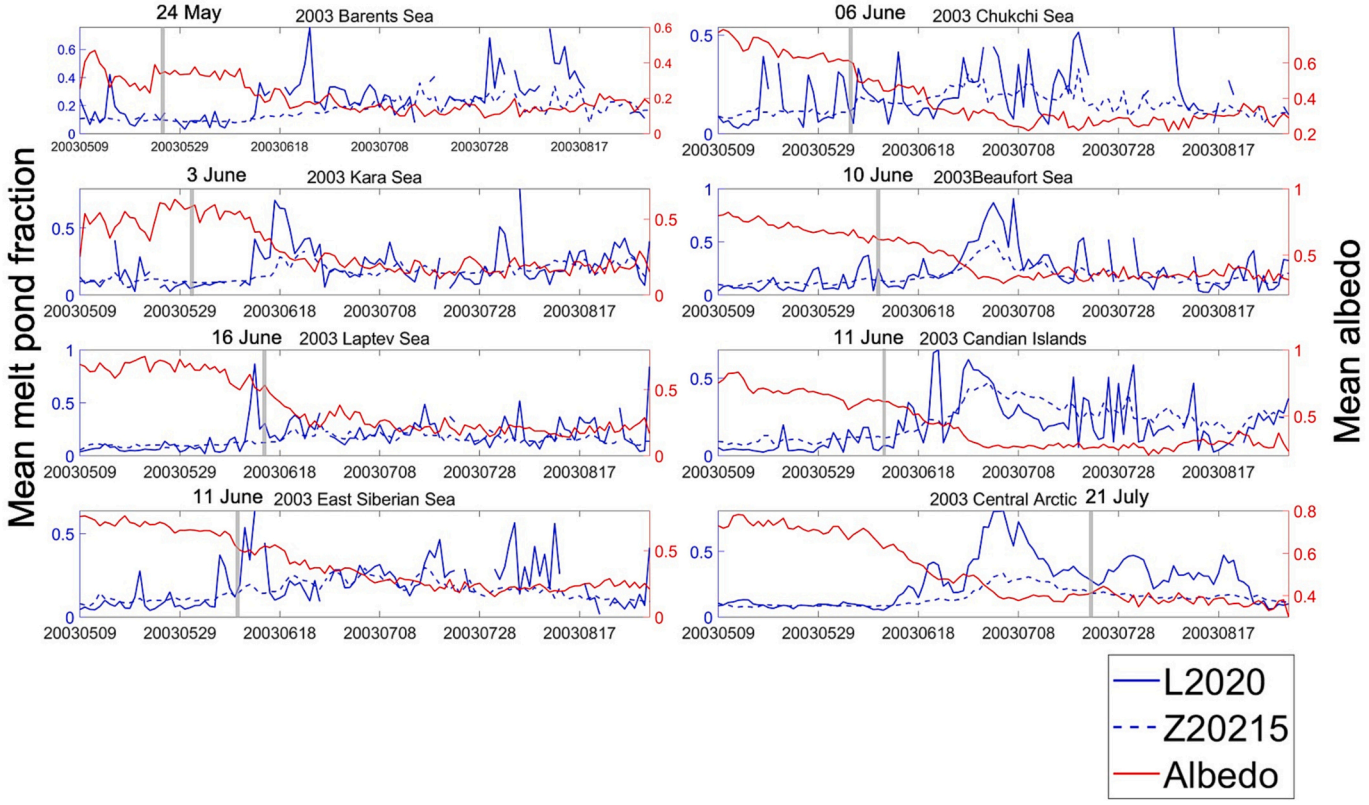

Fig. 16. Daily regional mean melt pond and albedo based on NSIDC Arctic regional mask from 9 May to 31 August 2003. Grey columns indicate mean melt onset date. Albedo evolution stages are illustrated with melt pond fractions in Central Arctic in 2003.

based melt pond products, yet they differ in method, spatial and temporal resolution, resulting in stark differences in pond fraction and interannual variability. This paper intercompares three publicly available melt pond products, Rösel et al. (2012), Lee et al. (2020) and Zege et al. (2015).

These different products are at times in agreement, especially early in the melt season, but they start to deviate as the melt season progresses, with the melt pond product of Lee et al. (2020) having considerably larger melt pond fractions in June and August. In a sense, increased melt pond fractions in August are in agreement with trends towards later freeze-up (e.g. Stroeve and Notz, 2018), and thus one would expect ponds still cover the ice in August. It is important to note however that none of the three melt products indicate a significant change in melt pond fractions between 2002 and 2011 except in July; L2020 further shows positive trend in melt pond fractions in August. However, none of the trends are statistically significant.

Comparison of the coarser resolution melt pond fraction estimates with high resolution satellite images such as Landsat and WorldView reveals that R2012 generally has the lowest melt pond fractions and may be most accurate in May. However, for the other summer months this algorithm underestimates pond fractions and we find that L2020 best matches WV-derived pond fractions in June and July in part because of the higher spatial resolution. However, while the higher spatial resolution data set of L2020 better captures the spatial distribution of WV-derived pond fractions, it does at times suffer from biases as a result of flooded ice, thin ice and/or leads misclassified as ponds. For spatial correlation between monthly melt pond fraction and albedo, Z2015 is the most negatively correlated, followed by R2012 and L2020. While the melt pond fraction on FYI generally is higher than on MYI, the difference is more pronounced in L2020 than R2012.

The purpose of this paper is to show the characteristics of current available melt pond products and provide a recommendation to the science community for user's needs. For further study, Artificial Intelligence (AI) approaches that consider the "shape" of melt ponds such as perimeter, fractal dimension, roundness, and convex degree could be developed to constrain the shape of expected melt ponds and perhaps separate out ponds over multiyear or rough ice from melt water over level ice.

Credit author statement

Sanggyun Lee: Conceptualization, Methodology, Software, Investigation, Writing-original draft, Writing-review & editing.

Julienne Stroeve: Conceptualization, Methodology, Writing-original draft, Writing-review & editing.

Melinda Webster: Providing Skysat images from MOSAiC and discussing data quality and availability, Writing-review & editing.

Niels Fuchs: Providing helicopter-borne images from MOSAiC and discussing data quality and availability, Writing-review & editing.

Donald Perovich: Providing Skysat images from MOSAiC and discussing data quality and availability.

Declaration of Competing Interest

The authors declare that they have no known competing financial interests or personal relationships that could have appeared to influence the work reported in this paper.

Data availability

All data used in this study are publicly available at the following URL: R2012 (https://www.cen.uni-hamburg.de/en/icdc/data/cryosphere/arctic-meltponds.html), Z2015 (https://seaice.uni-bremen.de/melt-ponds/) L2020 (http://www.cpom.ucl.ac.uk/melt_pond/ and https://data.bas.ac.uk/full-record.php?id=GB/NERC/BAS/PDC/01444). Helicopter derived surface type maps are available on

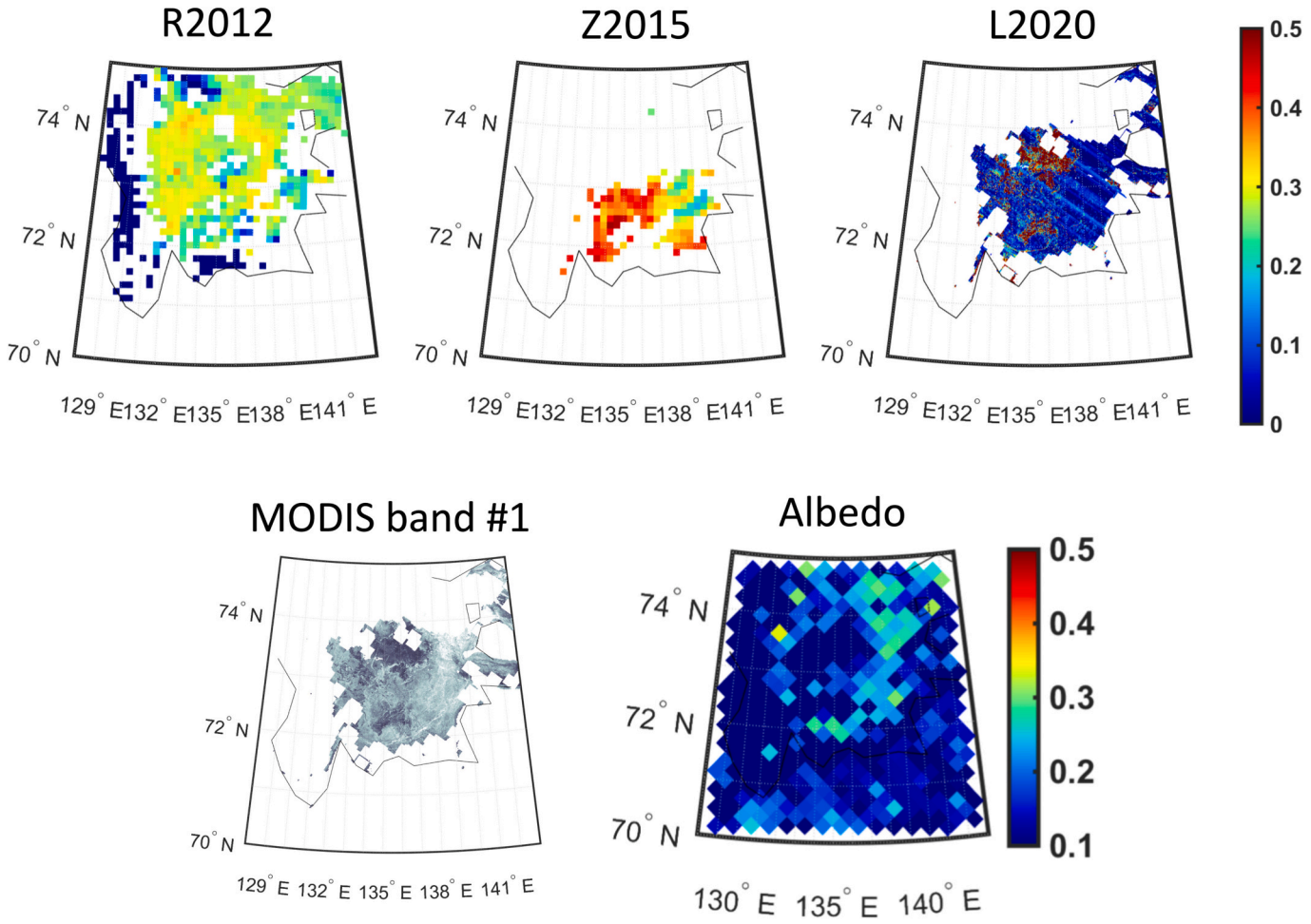

Fig. 17. Spatial comparison against albedo on 13 July 2003 around East Siberian Sea. 8-day composited (12–19 July 2003) melt pond fraction from R2012 at 12.5 km spatial resolution.

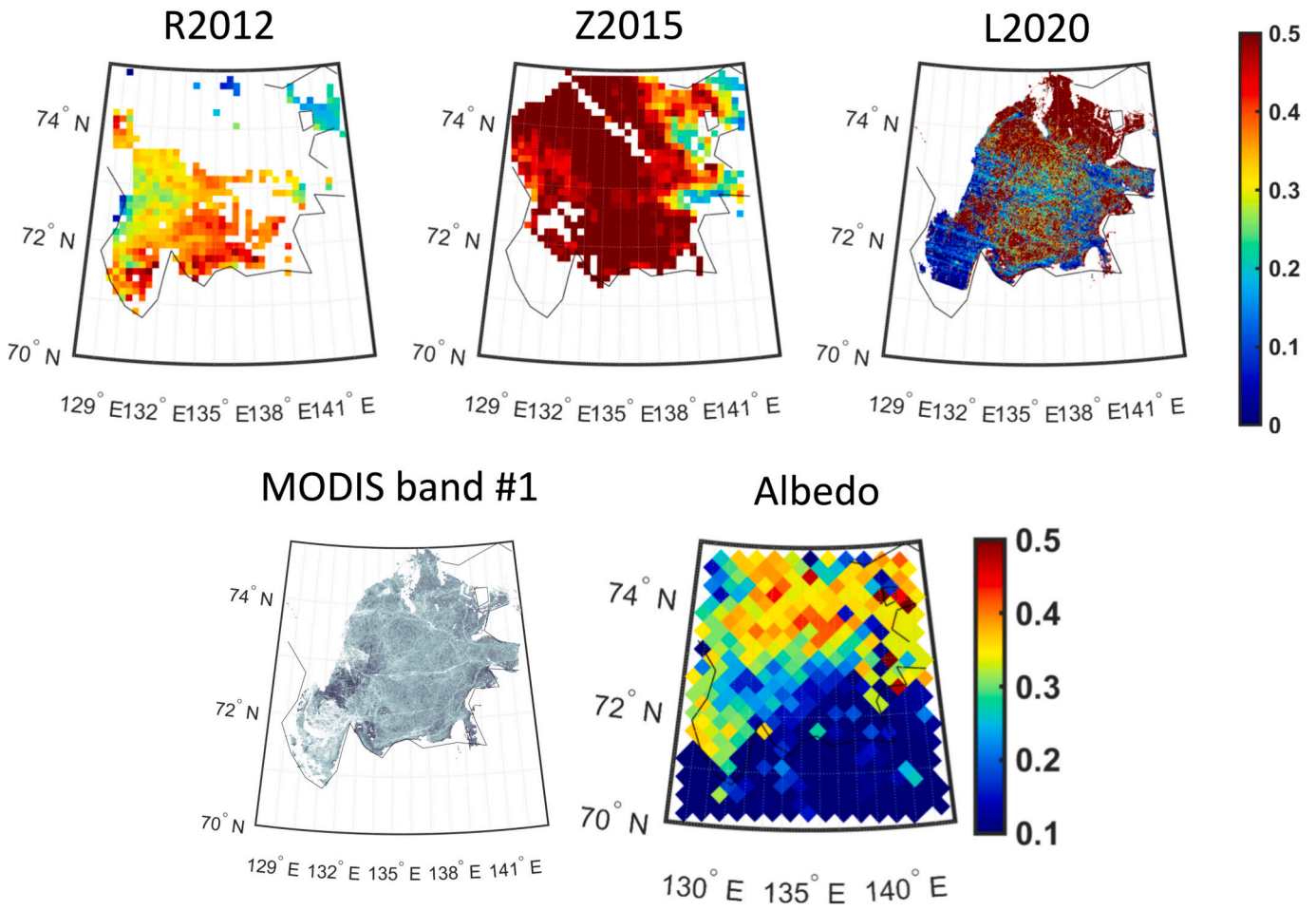

Fig. 18. Spatial comparison against albedo on 17 June 2010 around East Siberian Sea. 8-day composited (10–17 June 2010) melt pond fraction from R2012 at 12.5 km spatial resolution.

PANGAEA (https://doi.org/10.1594/PANGAEA.949167).

Acknowledgements

This work was funded by NERC grant NE/R017123/1, part of the joint NSFGEO-NERC Advancing Predictability of Sea Ice: Phase 2 of the Sea Ice Prediction Network, and by NASA grant NNX14AO07G. M.W. conducted this work under the National Science Foundation Project 2325430 and NASA's Interdisciplinary Research in Earth Science project 80NSSC21K0264. NF was supported by the German Ministry for Education and Research (BMBF) through the project NiceLABpro (Grant 03F0867A) We thank Nicholas Wright for the troubleshooting of WV-derived melt pond classification.

Appendix A. Supplementary data

Supplementary data to this article can be found online at https://doi.org/10.1016/j.rse.2023.113920.

References

Aaboe, S., Down, E.J., Eastwood, S., 2021. Algorithm theoretical basis document for the global. Sea-ice edge and type product. Version 3.3, Tech. rep. SAF/OSI/CDOP3/MET-Norway/SCI/MA/379. EUMETSAT Ocean and Sea Ice SAF.

Curry, J.A., Schramm, J.L., Ebert, E.E., 1995. Sea ice-albedo climate feedback mechanism. J. Clim. 8 (2), 240–247.

Diaz, A., Ehn, J.K., Landy, J.C., Else, B.G.T., Campbell, K., Papakyriakou, T.N., 2018. The energetics of extensive meltwater flooding of level Arctic Sea ice. J. Geophys. Res. Oceans 123, 8730–8748. https://doi.org/10.1029/2018JC014045.

Eicken, H., Grenfell, T.C., Perovich, D.K., Richter-Menge, J.A., Frey, K., 2004. Hydraulic controls of summer Arctic pack ice albedo. J. of Geo Res. Oceans 109.

Fetterer, F., Untersteiner, N., 1998. Observations of melt ponds on Arctic Sea ice. J. of Geo. Res.: Oceans 103, 24821–24835.

Flocco, D., Feltham, D.L., Turner, A.K., 2010. Incorporation of a physically based melt pond scheme into the sea ice component of a climate model. J. of Geo. Res.: Oceans 115.

Flocco, D., Schroeder, D., Feltham, D.L., Hunke, E.C., 2012. Impact of melt ponds on Arctic Sea ice simulations from 1990 to 2007. J.l of Geo. Res.: Oceans 117.

Fuchs, N., 2023. A Multidimensional Analysis of Sea Ice Melt Pond Properties from Aerial Images (Doctoral dissertation. Universität Bremen.

Fuchs, N., Birnbaum, G., 2023. Orthomosaics and surface type classifications of MOSAiC leg 4 floe (2020-06-30, 2020-07-22). PANGAEA. https://doi.org/10.1594/PANGAEA.949167.

Horvat, C., Jones, D.R., Iams, S., Schroeder, D., Flocco, D., Feltham, D., 2017. The frequency and extent of sub-ice phytoplankton blooms in the Arctic. Oce. Sci. Adv. 3, e1601191.

Hunke, E.C., Hebert, D.A., Lecomte, O., 2013. Level-ice melt ponds in the Los Alamos Sea ice model. CICE. Oce. Model. 71, 26–42.

Key, J., Wang, X., Liu, Y., Dworak, R., Letterly, A., 2016. The AVHRR polar pathfinder climate data records. Rem. Sens. 8, 167.

Lee, S., Stroeve, J., Tsamados, M., Khan, A.L., 2020. Machine learning approaches to retrieve pan-Arctic melt ponds from visible satellite imagery. Rem. Sens. of Env. 247, 111919.

Light, B., Smith, M.M., Perovich, D.K., Webster, M., Holland, M.M., Linhardt, F., Bailey, D.A., 2022. Arctic Sea ice albedo: spectral composition, spatial heterogeneity, and temporal evolution observed during the MOSAiC drift. Elem. Sci. Anth. 10 (1), 000103.

Liu, J., Song, M., Horton, R.M., Hu, Y., 2015. Revisiting the potential of melt pond fraction as a predictor for the seasonal Arctic Sea ice extent minimum. Env.Res. Let. 10, 054017.

Nicolaus, M., Hudson, S.R., Gerland, S., Munderloh, K., 2010. A modern concept for autonomous and continuous measurements of spectral albedo and transmittance of sea ice. Co. Reg. Sci. and Tech. 62, 14–28.

Niels, Fuchs, 2023. A Multidimentional Analysis of Sea Ice Melt Pond Properties from Aerial Images (doctoral dissertation, Universität Bremen).

Perovich, D.K., Polashenski, C., 2012. Albedo evolution of seasonal Arctic Sea ice. Geo. Res. Let. 39 (8).
Perovich, D.K., Light, B., Eicken, H., Jones, K.F., Runciman, K., Nghiem, S.V., 2007. Increasing solar heating of the Arctic Ocean and adjacent seas, 1979–2005: Attribution and role in the ice-albedo feedback. Geo. Res. Let. 34.
Polashenski, C., Perovich, D., Courville, Z., 2012. The mechanisms of sea ice melt pond formation and evolution. Jou. of Geo. Res.: Oceans 117 (C1).
Romanov, R., 1995. Atlas of Ice and Snow of the Arctic Basin and Siberian Shelf Seas, Backbon,2 Edn. New York.
Rösel, A., Kaleschke, L., Birnbaum, G., 2012. Melt ponds on Arctic Sea ice determined from MODIS satellite data using an artificial neural network. The Cryo. 6, 431–446.
Schröder, D., Feltham, D.L., Flocco, D., Tsamados, M., 2014. September Arctic Sea-ice minimum predicted by spring melt-pond fraction. Nat. Clim. Cha. 4, 353–357.
Stroeve, J.C., Markus, T., Boisvert, L., Miller, J., Barrett, A., 2014. Changes in Arctic melt season and implications for sea ice loss. Geo. Res. Let. 41, 1216–1225.
Stroeve, J.C., Nandan, V., Willatt, R., Dadic, R., Rostosky, P., Gallagher, M., Mallett, R., Barrett, A., Hendricks, S., Tonboe, R., McCrystall, M., Serreze, M., Thielke, L., Spreen, G., Newman, T., Yackel, J., Ricker, R., Tsamados, M., Macfarlane, A., Hannula, H.-R., Schneebeli, M., 2022. Rain on snow (ROS) understudied in sea ice remote sensing: a multi-sensor analysis of ROS during MOSAiC (multidisciplinary drifting Observatory for the Study of Arctic climate). Cryosphere 16, 4223–4250.
Stroeve, J., Notz, D., 2018. Changing State of Arctic Sea Ice Across All Seasons. Env. Rea. Let. 13 (10), 103001.
Tanaka, Y., 2020. Estimating meltwater drainage onset timing and duration of landfast ice in the Canadian arctic archipelago using AMSR-E passive microwavendata. Rem. Sens. 12 (6), 1033.
Taylor, C., Boeke, C., Li, Y., Thompson, D., 2019. Arctic Cloud Annual Cycle Biases in Climate Models. Atmospheric Chemistry and Physics 19 (13), 8759–8782.
Tschudi, M.A., Maslanik, J.A., Perovich, D.K., 2008. Derivation of melt pond coverage on Arctic sea ice using MODIS observations. Rem. Sens. of Env. 112, 2605–2614.
Wright, N.C., Polashenski, C.M., 2018. Open-source algorithm for detecting sea ice surface features in high-resolution optical imagery. The Cryo. 12, 1307–1329.
Wright, N., Webster, M., Polashenski, C., 2021. Melt Pond Maps around the. Multidisciplinary Drifting Observatory for the Study of Arctic Climate (MOSAiC) Drifting Station Derived from High Resolution Optical Imagery. Arctic Data Center. https://doi.org/10.18739/A2696ZZ9W.
Zege, E., Malinka, A., Katsev, I., Prikhach, A., Heygster, G., Istomina, L., Birnbaum, G., Schwarz, P., 2015. Algorithm to retrieve the melt pond fraction and the spectral albedo of Arctic summer ice from satellite optical data. Rem. Sen. of Env. 163, 153–164.